Astronomy & Astrophysics manuscript no. paper-pks-ATCA7mm-final
January 19, 2013
© ESO 2013

arXiv:1104.3361v2 [astro-ph.CO] 20 Sep 2011

Molecules at z=0.89:
A 4-mm-rest-frame absorption-line survey toward PKS 1830−211

S. Muller[1], A. Beelen[2], M. Guélin[3,4], S. Aalto[1], J. H. Black[1], F. Combes[5], S. J. Curran[6], P. Theule[7], and S. N. Longmore[8]

[1] Onsala Space Observatory, SE 439-92, Onsala, Sweden
[2] Institut d'Astrophysique Spatiale, Bât. 121, Université Paris-Sud, 91405 Orsay Cedex, France
[3] Institut de Radioastronomie Millimétrique, 300, rue de la piscine, 38406 St Martin d'Hères, France
[4] Ecole Normale Supérieure/LERMA, 24 rue Lhomond, 75005 Paris, France
[5] Observatoire de Paris, LERMA, CNRS, 61 Av. de l'Observatoire, 75014 Paris, France
[6] School of Physics, University of New South Wales, Sydney NSW 2052, Australia
[7] Physique des interactions ioniques et moléculaires, Université de Provence, Centre de Saint Jérôme, 13397 Marseille Cedex 20, France
[8] ESO, Karl-Schwarzschild-Str. 2, 85748 Garching, Germany

Received / Accepted

ABSTRACT

We present the results of a 7 mm spectral survey of molecular absorption lines originating in the disk of a z=0.89 spiral galaxy located in front of the quasar PKS 1830−211. Our survey was performed with the Australia Telescope Compact Array and covers the frequency interval 30–50 GHz, corresponding to the rest-frame frequency interval 57–94 GHz. A total of 28 different species, plus 8 isotopic variants, were detected toward the south-west absorption region, located about 2 kpc from the center of the z=0.89 galaxy, which therefore has the largest number of detected molecular species of any extragalactic object so far. The results of our rotation diagram analysis show that the rotation temperatures are close to the cosmic microwave background temperature of 5.14 K that we expect to measure at z=0.89, whereas the kinetic temperature is one order of magnitude higher, indicating that the gas is subthermally excited. The molecular fractional abundances are found to be in-between those in typical Galactic diffuse and translucent clouds, and clearly deviate from those observed in the dark cloud TMC 1 or in the Galactic center giant molecular cloud Sgr B2. The isotopic ratios of carbon, nitrogen, oxygen, and silicon deviate significantly from the solar values, which can be linked to the young age of the z=0.89 galaxy and a release of nucleosynthesis products dominated by massive stars. Toward the north-east absorption region, where the extinction and column density of gas is roughly one order of magnitude lower than toward the SW absorption region, only a handful of molecules are detected. Their relative abundances are comparable to those in Galactic diffuse clouds. We also report the discovery of several new absorption components, with velocities spanning between −300 and +170 km s^{-1}. Finally, the line centroids of several species (e.g., CH_3OH, NH_3) are found to be significantly offset from the average velocity. If caused by a variation in the proton-to-electron mass ratio μ with redshift, these offsets yield an upper limit $|\frac{\Delta\mu}{\mu}|<4\times10^{-6}$, which takes into account the kinematical noise produced by the velocity dispersion measured from a large number of molecular species.

Key words. quasars: absorption lines - quasars: individual: PKS 1830−211 - galaxies: ISM - galaxies: abundances - ISM: molecules

1. Introduction

More than 150 molecules have been discovered in space, as a result of targeted investigations or spectral surveys toward Galactic sources such as circumstellar envelopes of evolved stars (e.g. IRC+10216, Cernicharo et al. 2000; Patel et al. 2011), massive star-forming clouds (e.g. Sgr B2, Nummelin et al. 2000), or cold molecular clouds (e.g. TMC-1, Ohishi et al. 1992; Kaifu et al. 2004). The study of the rotational and vibrational spectra of these molecules is particularly useful to probe the physical conditions and chemical content of the interstellar gas. Most importantly, the large number of molecules found in various environments demonstrates the richness and variety of interstellar chemistry.

As the sensitivity of millimeter instruments has increased, a large number of molecules have become observable in galaxies in the Local Universe (see e.g. Wang et al. 2004; Martín et al. 2006 for NGC4945 and NGC253, respectively) and molecules are still detected at high redshifts (currently up to z=6.42), though only a few species such as CO, HCN, HCO$^+$, and HNC (e.g. Walter et al. 2003; Wagg et al. 2005; Riechers et al. 2006; Guélin et al. 2007). Those detections are mostly related to ultra-luminous galaxies, which are potentially unrepresentative of all galaxies at these epochs. Moreover, line emission from these high-z galaxies is dominated by the warmest and densest regions of the molecular component.

Observations of molecular absorption lines toward a bright radio continuum source allow rare molecular species to be detected even in distant galaxies, where they cannot be observed in emission because of distance dilution. This technique can thus be used to investigate the chemistry and its complexity at high redshifts and trace the chemical enrichment history of the Universe. In addition, high-z molecular absorbers can serve as cosmological probes of the cosmic microwave background (CMB) temperature and have attracted much interest in constraining variations in the fundamental constants of physics (see e.g., Henkel et al. 2009 and references therein).

Unfortunately, only a handful of high-redshift radio molecular absorbers [1] have been discovered to date (see the review by Combes 2008), despite numerous searches (e.g. Wiklind & Combes 1996a; Drinkwater et al. 1996; Murphy et al. 2003; Curran et al. 2004, 2006, see also Curran et al. 2011). The molecular absorption originating in the z=0.89 and z=0.68 intervening galaxies located in front of the quasars PKS 1830−211 (z=2.5) and B 0218+357 (z=0.94) respectively, were discovered by Wiklind & Combes (1995, 1996b) and have many similarities: both absorbers appear to be (faint) nearly face-on spiral galaxies (Winn et al. 2002; York et al. 2005); both galaxies act as gravitational lenses and split the image of their background quasar into two main compact components and an Einstein ring, as seen at radio wavelengths (Jauncey et al. 1991; Patnaik et al. 1993); they both harbor large column densities of absorbing molecular gas ($N(H_2) > 10^{22}$ cm^{-2}); and in both cases the radio continuum of the background quasar is bright enough to permit sensitive observations with current millimeter instruments. A dozen molecular species have indeed been successfully detected in these absorbers, as well as absorption by their rare isotopologues (cf e.g., Wiklind & Combes 1995, 1996b, 1998; Menten et al. 1999; Muller et al. 2006).

The multiplicity of lensed continuum images of the background quasar makes it possible to explore as many different lines of sight through the intervening galaxy. In the case of B 0218+357, molecular absorption is detected only toward one image of the quasar (Menten & Reid 1996; Muller et al. 2007). Toward PKS 1830−211, molecular absorption is detected, however, for both of the bright and compact images, located one arcsecond apart on the north-east and south-west side, respectively, of the Einstein ring (Wiklind & Combes 1998; Muller et al. 2006). The two lines of sight intercept the disk of the z=0.89 galaxy (hereafter referred to as FG0.89, where FG stands for foreground galaxy) on either side of its bulge, at galactocentric distances of ∼2 kpc (to the SW) and ∼4 kpc (to the NE). An image of the galaxy, obtained with the Hubble Space Telescope in the I band is shown in Fig.1.

The absorption toward the SW image (hereafter FG0.89SW) has a large column of absorbing gas ($N(H_2) > 10^{22}$ cm^{-2}) and is taken as the reference 0 km s^{-1} in velocity (z=0.88582, Wiklind & Combes 1996b). Remarkably, the full width at zero power of the HCO$^+$(2-1) line reaches nearly 100 km s^{-1} for this component, although the galaxy is seen almost face-on. We note the relatively high kinetic temperature of ∼80 K (Henkel et al. 2008) and moderate density of a few times 10^3 cm^{-3} (Henkel et al. 2009) toward FG0.89SW, which imply that the excitation of the rotational lines is subthermal and mostly, but not necessarily totally, coupled with the CMB. Rotation temperatures derived for several molecules are consistent with the value T_{CMB}=5.14 K at z=0.89 (Combes & Wiklind 1997; Menten et al. 1999; Henkel et al. 2009), as predicted for an adiabatic expansion of the Universe.

The absorption toward the NE component (hereafter FG0.89NE) is located ∼147 km s^{-1} blueward and is narrower (FWHM∼15 km s^{-1}), so that both velocity components can easily be resolved kinematically. Nevertheless, the column of molecular gas toward the NE image is about two orders of magnitude less than in FG0.89SW, and the corresponding absorption lines are significantly weaker. Little is known about the excitation of and the physical conditions toward FG0.89NE. However, based on the analysis of time variations in the NE absorption, Muller & Guélin (2008) argued that it should be caused by a small number ($\leq$5) of clouds of size ∼1 pc and of density a few 100 cm^{-3}, hence resembling Galactic diffuse clouds.

Molecular absorption has also been detected in the galaxies hosting the radio sources B3 1504+377 at z=0.67 (in CO, HCO$^+$, HCN, and HNC; Wiklind & Combes 1996b), PKS 1413+135 at z=0.25 (in CO, HCO$^+$, HCN, HNC, and CN; Wiklind & Combes 1997), and PKS 0132−097 at z=0.76 (although only in OH; Kanekar et al. 2005). However, the weakness of the background radio continuum sources, narrower linewidths and smaller column densities of absorbing gas than the two absorbers toward PKS 1830−211 and B 0218+357, ensures that it is difficult to perform a deep inventory of their molecular constituents with current instruments.

In this paper, we present the first unbiased spectral-line survey toward a high-z molecular absorber, located at z=0.89 in front of the quasar PKS 1830−211. Observations, conducted with the Australian Compact Array and covering the whole 7 mm band from 30 GHz to 50 GHz, are presented in §.2. Our results are presented in §.3, and then discussed in §.4, in terms of isotopic ratios (§.4.1), the chemical composition relative to other objects (§.4.2), and constraints on the variation in fundamental constants of physics (§.4.3). Notes for the different molecular species detected in the survey are given in appendix.

2. Observations and data reduction

Observations were carried out with the Australian Telescope Compact Array (ATCA) over three nights, on 2009 September 1 and 2 and on 2010 March 17 (see Table 1). The array was in the EW352 and H168 configuration, respectively, and we used the five inner antennas, discarding the sixth one located 4 km away as we obtained unsatisfactory pointing solutions and data quality. The maximum baseline length was then up to 352 m and 192 m in either configuration, respectively. With this configuration, PKS 1830−211 was mostly unresolved, and is further considered as a point-like source. The weather was clear in both runs.

For each tuning, the bright quasar 1923−293 was observed for several minutes to help us perform bandpass calibration, and the pointing was checked and updated against PKS 1830−211, before integrating. We did not observe gain calibrators, as PKS 1830−211 visibilities were self-calibrated and the continuum level normalized to unity.

The Compact Array Broadband Backend (CABB) system was configured to provide a 1 MHz spectral resolution

---

[1] That is, not including the H_2/CO absorbers detected from optical/UV spectroscopy, such as those discussed in Noterdaeme et al. (2011).

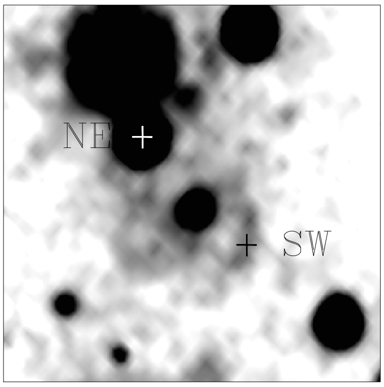

Fig. 1. Image of the z=0.89 galaxy obtained with the Hubble Space Telescope in the I band (see also Muller et al. 2006). The positions of the SW and NE images of the quasar are indicated. The distance between them is one arcsecond. Note the high extinction toward the SW image of the quasar, produced by the interstellar medium of the intervening galaxy.

per 2 GHz window with dual polarization. Two windows were used simultaneously, with central frequencies set as reported in Table 1. The whole 7 mm band (30–50 GHz) could then be covered in a fairly small number of individual tunings. Each part of the band was covered in at least two tunings, in order to prevent potential defectuous spectral channels. Some parts of the spectral band were indeed affected by a series of bad channels, as can be seen for example in the final spectrum between 40 and 40.2 GHz in Fig.A.1. Some frequency intervals were observed in more tunings, to increase the sensitivity, for example at the frequencies of the deuterated species DCO$^+$ and DCN. The spectral resolution of 1 MHz corresponds to ∼10 km s^{-1} at 30 GHz and ∼6 km s^{-1} at 50 GHz.

The data reduction was performed in two steps. We used the MIRIAD package for a first bandpass calibration adopting the solution derived from 1921-293 and the self-calibration of the PKS 1830−211 data. At this step, the analysis of each 2-GHz spectral window revealed a residual bandpass, with amplitudes roughly varying by an order of one percent over several 100 MHz. To remove this bandpass drift residuals – the final sensitivity being of about a few times 10^{-3} only –, data were then exported to FITS format and subsequently processed with a customised ITT/IDL pipeline.

The pipeline is based on an iterative boxcar drift removal. Each iteration was designed to construct a model spectrum (i.e., a spectrum with any slow variations in the bandpass removed) from the raw data following several steps:

- first, for each observed tuning, each polarization and each baseline, we flagged outliers in time by assuming that the visibilities were constant on timescales longer than ten seconds;
- a drift component was then computed and removed, in both time and frequency with different windows widths, taking proper care of any flagged or missing data;
- a first crude spectrum, after evaluating the time-averaged visibilities, was obtained and its residuals were used to find frequency channels with large deviations from a random Gaussian distribution;
- at this stage, we also examined the spectra for each antenna, to check for possible antenna-based problems;
- the standard deviation of each baseline was then used to compute a weighted mean spectrum and the uncertainty for each tuning and polarization;
- finally, a Doppler track correction was applied according to the observatory velocities given in Table 1, obtained from the ATCA frequency calculator [2]. All velocities in this paper refer to the Solar System barycenter rest-frame. We note that the Doppler correction is nearly constant during the short observing intervals for individual tunings. Data were accordingly re-gridded onto a common frequency scale using a one-dimensional (1D) drizzling algorithm (Fruchter & Hook 2002). We tested different frequency resolutions and chose a channel width of 0.5 MHz. A weighted mean was finally used to combine all spectra.

A model of the spectrum was derived by finding all frequency channels above a given threshold. This model was then removed from the data, and the whole process was iterated on the residual datasets.

We started with a large width for the bandpass residual filtering, corresponding roughly to 1 GHz, and a high threshold of 10 σ to derive the model. The pipeline was run until the variance of the resulting spectrum was found to have reached a minimum. The model threshold was lowered iteratively in steps of two down to 4 σ in order to correct for the negative corrections of the boxcar drift removal on strong lines. Following the same scheme, the filtering width was successively divided by two until it reached a width of 16 MHz.

This whole procedure ensures that the second order bandpass is removed, without making any *a priori* assumptions about the presence of strong absorption lines. The resulting spectrum is shown in Fig.A.1.

3. Results and analysis

An overview of the 20-GHz-wide resulting spectrum is shown in Fig.2. The frequency coverage corresponds, in the rest frame of the z=0.89 galaxy, to the range 57–94 GHz. The lower end of this frequency interval is relatively unexplored because of poor atmospheric transmission caused by a forest of fine-structure lines of O_2 around 60 GHz. The rms noise level is not uniform over the whole band, and varies owing to the higher system temperatures at higher frequencies and the different integration times. The full survey is presented in Fig.A.1.

Only a handful of absorption lines reach an optical depth of 10% (see Eq.1) or more. They originate in the SW absorption component and correspond, in order of decreasing optical depth, to: HCO$^+$, HCN, HNC, C_2H, N_2H^+, H_2CO, c-C_3H_2, and H^{13}CO$^+$. All these species have been detected in previous observations (Wiklind & Combes 1998; Menten et al. 1999). The weaker NE absorption at $V \sim -147$ km^{-1} is detected only for HCO$^+$, HCN, HNC, C_2H, c-C_3H_2, and H_2CO.

The major result of this survey, though, is the detection of a collection of weak absorption lines toward the SW com-

---

[2] http://www.narrabri.atnf.csiro.au/observing/obstools/velo.html

Table 1. Journal of the observations.

Freq. (GHz)	Time (UT)	Δt (h)	V_{obs} (km s^{-1})
2009 September 1			
31 & 33	6:49	0.8	+25.71
37 & 39	8:14	1.2	+25.84
44 & 47.5	10:00	1.5	+26.03
42 & 46.5	11:56	1.6	+26.23
35 & 38	13:32	0.9	+26.36
2009 September 2			
32 & 34	6:44	0.8	+25.95
41 & 45	8:08	1.2	+26.07
46.5 & 49	10:19	1.4	+26.30
43 & 47	11:55	1.0	+26.47
36 & 38.5	13:10	0.7	+26.57
2010 March 17			
37.25 & 40	19:16	3.0	−29.44
46.1 & 48.1	22:22	3.0	−29.16

Notes. Frequencies indicate the center of each 2 GHz ATCA/CABB bands; time is given at the middle of the time interval Δt spent on the frequency tuning, and V_{obs} is the observatory velocity used to perform Doppler correction (with respect to the Solar System barycenter rest-frame).

ponent, down to a few times 10^{-3} of the continuum intensity, as illustrated in Fig.3, where the cumulative number of detected lines is plotted as a function of opacity. These lines were identified using the on-line Cologne Database for Molecular Spectroscopy[3] (CDMS, Müller et al. 2001), and Jet Propulsion Laboratory Molecular Spectroscopy Database [4] (JPL, Pickett et al. 1998). The corresponding transitions are listed in Table A.1.

All detected transitions (except the $K > 1$ transitions of CH_3CN, see §.B.14) are ground state or have low energy levels. Most molecules have high dipole moments, and the gas density is too moderate for collisions to play an efficient role in the excitation. Rotational transitions are therefore nearly in radiative equilibrium with the CMB, which has a temperature of ∼5 K at z=0.89. Several species are detected in more than one transition, and a rotation diagram analysis indeed yields rotation temperatures in agreement with this value. A low energy level is therefore a good filter to identify transitions/species in the molecular databases, and this is why we believe that our identifications are robust, even for species with a single detected transitions. The confusion is also low, with a rough average of four clear lines per GHz over the 20-GHz-wide band.

The census of molecules detected to date in the z=0.89 galaxy located in front of PKS 1830−211 is given in Table 3. It is quite remarkable that, despite its distance, this z=0.89 galaxy has now become the object with the largest number of detected molecules outside the Milky Way. A large fraction of the total number of these species (28 out of 34) are detected in our survey, among them 19 for the first time toward this source. As far as we know, this work also represents the first extragalactic detection for SO^+, l-C_3H, l-C_3H_2, H_2CCN, H_2CCO, C_4H, CH_3NH_2, and CH_3CHO. In addition, isotopologues of HCO^+, HCN, HNC, and SiO were also detected. Elemental isotopic ratios of C, N, O, and Si are derived and discussed in §4.1.

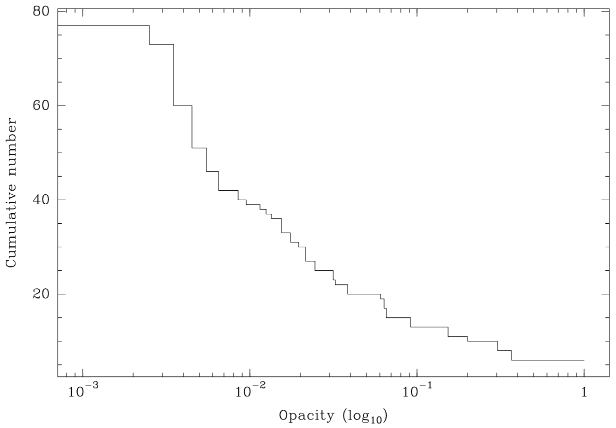

Fig. 3. Cumulative number of lines detected toward FG0.89SW with optical depths higher than a specified value.

3.1. Fitting procedure

We fitted a Gaussian profile to all the transitions of a given species with a single velocity and a single linewidth. The ortho and para forms, when relevant, were considered as the same species for the fit. The relative intensities of all species with resolved or marginally resolved hyperfine structure were fixed, as it was observed that, in the case of C_2H and HCO (for which the hyperfine structure is clearly resolved), they follow the predicted ratios assuming local thermal equilibrium (LTE). The velocity and linewidth of isotopic variants were fixed relative to the main isotopologue, except for HCO^+ and HCN, the lines of which are likely saturated. For these, the corresponding isotopic variants were instead fixed relative to $H^{13}CO^+$ and $H^{13}CN$. For some species with data for the various transitions of low signal-to-noise ratio (S/N), we decided to fix the velocity (e.g. l-C_3H_2) or the linewidth (e.g. SO^+) after initial free fits. Finally, the fit for CH_3CN is degenerate because of the blending of the K=0 and K=1 transitions, and for this species, we therefore chose to adjust a synthetic spectrum by eye. The fitting results are given in Table A.1.

3.2. Time variations

A monitoring of the HCO^+ J=2-1 absorption profile between 1995 and 2008 revealed significant time variations (Muller & Guélin 2008), in particular with the quasi-disappearance of the −147 km s^{-1} absorption component between 2006 to 2007. In the HCO^+ J=2-1 spectrum acquired by Muller & Guélin in October 2008 with the Plateau de Bure interferometer, this component had returned with an absorption of ∼15% of the total continuum intensity. Variations were found to be correlated between the −147 km s^{-1} component and the blue wings of the 0 km s^{-1} absorption, hence should originate from morphological changes in the background quasar.

From Very Long Baseline Interferometry continuum measurements, the relative distance between the NE and

---

[3] http://www.astro.uni-koeln.de/cdms

[4] http://spec.jpl.nasa.gov/home.html

SW lensed images of the quasar was found to vary by as much as 200 micro-arcseconds within a few months (Jin et al. 2003). Nair et al. (2005) proposed that this apparent motion is caused by the sporadic ejection of plasmons along a helical jet by the quasar. Consequently, the continuum illumination scans different pencil beams through the foreground absorbing clouds, where the apparent displacement of the quasar lensed images corresponds to a projected distance of about a parcsec, i.e. a scale comparable to the size of Galactic molecular-cloud cores.

The relative differences (normalized to the averaged spectrum) for the spectral regions covered in both runs (September 2009 and March 2010) are shown together with the averaged spectrum in Fig.A.1. They are at most ∼5% for the HCO^+, HCN, and HNC lines, and barely visible for all other lines. Given the small relative changes, data from both observing sessions were combined to improve the S/N of the data.

3.3. Background continuum illumination

Absorption intensities (I_ν), measured from the continuum level, were converted to optical depths (τ_ν) according to

$$\tau_\nu = -\ln\left(1 - \frac{I_\nu}{f_c I_{bg}}\right), \tag{1}$$

where I_{bg} is the intensity of the background continuum source, and f_c the source covering factor. At radio wavelengths, the continuum emission of the quasar PKS 1830−211, lensed by the z=0.89 intervening galaxy, is dominated by two bright and compact components (to the NE and SW), separated by 1" and included in an overall fainter Einstein ring. The flux ratio of the NE to SW compact components is ∼1.5–1.6 at cm wavelengths as measured by Subrahmanyan et al. (1990). The remaining emission (Einstein ring and fainter other components) contributes only to a few percent of the total continuum intensity.

Molecular absorption in the z=0.89 galaxy is observed toward both the SW and NE continuum images. The HCO^+ J=2-1 absorption toward the SW image shows a flat-bottom profile, indicating saturation. Assuming that, at this wavelength, all the continuum emission comes from the NE and SW images of the quasar, it is then possible to derive the relative flux NE/SW of both images from the level of this saturation, without actually resolving them. The NE/SW ratio was measured to be about 1.7 with a dispersion of 0.3 over several observations between 1995 and 2007 (Muller & Guélin 2008), i.e. roughly similar to the flux ratio directly measured at cm wavelengths. Some of the fluctuations might be due to morphological changes in the quasar (plasmon burst, microlensing) and the time delay between the two line of sights.

Our 7 mm survey is limited in terms of spectral resolution, and the flat-bottom part of the HCO^+/HCN J=1-0 lines (supposing that they are also saturated) is smooth, preventing the same analysis. Nevertheless, as the HCO^+ $1-0$ absorption reaches an apparent depth of ∼35% and 8% toward the SW and NE components, relative to the total continuum level, we can certainly state that $0.35 < I_{bg}(\mathrm{SW}) < 0.92$ and $0.08 < I_{bg}(\mathrm{NE}) < 0.65$. If, in addition, we impose the ratio R =NE/SW, we get the stronger constraints of $0.35 < I_{bg}(\mathrm{SW}) < \frac{0.65}{R}$ and $0.35\times R < I_{bg}(\mathrm{NE}) < 0.65$, which gives $I_{bg}(\mathrm{NE})$=0.61±0.05 and $I_{bg}(\mathrm{SW})$=0.38 ± 0.03 with R=1.6. We adopt these values. The rough uncertainty in the illuminating background continuum for both NE and SW components is therefore less than 10%. The residual contribution from components other than the NE and SW images is *de facto* less than $[1 - 0.35 \times (1 + R)]$, that is 9% with R=1.6.

This is valid, of course, if no changes happened in the quasar within the time corresponding to the time delay between the two lines of sight (∼24 days) before our observations. Unfortunately, we do not have flux monitoring data corresponding to these epochs. Nevertheless, that we do not see significant variations in the absorption line profiles between the observations of September 2009 and March 2010 is reassuring.

We can now investigate how this uncertainty in the background continuum illumination propagates to the derivation of opacities, by means of Eq.1. In the case of weak lines ($I << I_{bg}$), we get $\frac{\Delta\tau}{\tau} = \frac{\Delta I_{bg}}{I_{bg}}$, and our opacities are therefore estimated more accurately than 10%. For the other lines, we get $\frac{\Delta\tau}{\tau} = \frac{\Delta I_{bg}}{I_{bg}} \times F(I/I_{bg})$, where the function $F(x) = x/((x-1)\ln(1-x))$, and tends to infinity for $x \to 1$, although the rise is slow, as $F(0.9)$ (that is $I/I_{bg} = 90\%$) is still < 4. For example, the corresponding uncertainty in HNC opacity (the third strongest absorption line in our survey, after HCO^+ and HCN) is less than 20%.

Finally, we assume here (as in the rest of the paper) a source covering factor f_c of unity for all absorption components. It is however possible that $f_c < 1$ and changes with frequency, as the continuum emission probably becomes more extended at lower frequencies (see also the discussion by Henkel et al. 2009). As a result, the optical depths derived from Eq.1 are, strictly speaking, lower limits. We note however that the HCO^+ and HCN J=2-1 lines toward the SW absorption are optically thick and saturated. The source covering factor for this component is thus certainly close to unity. Toward the NE absorption, the situation is not so clear. The formal observational constraints from the HCO^+ 1-0 line are $\tau > 0.14$ and $f_c > 0.13$. While the non-detection of $H^{13}CO^+$ (with $HCO^+/H^{13}CO^+>71$) suggests that the line is likely optically thin, the source covering factor is still only poorly constrained.

3.4. LTE analysis and rotation diagrams

For optically thin lines, and assuming a Boltzmann distribution characterized by a rotation temperature T_{rot}, column densities N_{col} can be derived as

$$N_{LTE} = \frac{3h}{8\pi^3\mu^2 S_{ul}} \frac{Q(T_{rot})\exp\left(\frac{E_l}{k_B T_{rot}}\right)}{\left[1 - \exp\left(\frac{-h\nu}{k_B T_{rot}}\right)\right]} \int \tau dV, \tag{2}$$

where $Q(T_{rot})$ is the partition function, E_l the energy of the lower level with respect to ground state, μ the dipole moment, ν the frequency, and S_{ul} the line strength. Under these conditions, the column density of a detected molecule can be calculated directly with the knowledge of only one physical parameter: the rotation temperature T_{rot}.

Since some species are detected in several transitions, an excitation analysis can be done. Under the Rayleigh-Jeans

(RJ) approximation ($h\nu << k_BT$), Eq.2 can be re-arranged as

$$\log\left(\frac{3k_B\int\tau dV}{8\pi^3\nu\mu^2S_{ul}}\right)=\log\left(\frac{N_{col}}{Q(T_{rot})T_{rot}}\right)-\frac{E_l\log(e)}{k_BT_{rot}}. \quad (3)$$

Plotting the quantity on the left side of this equation versus the energy of the lower level for each observed transition then allows the rotation temperature T_{rot} to be measured as the inverse of the slope of a linear fit to the data points in the rotation diagram. Column densities were also derived, following Eq.3, from the intercept of the y-axis in the rotation diagram. Because the uncertainties in the data points in the rotation diagrams do not follow a normal distribution, the rotation temperatures, column densities, and their corresponding uncertainties were estimated using Monte Carlo simulations. We note that the RJ approximation is still valid for $T > 4.5$ K at 94 GHz, the highest rest-frame frequency reached in our survey.

The rotation diagrams for molecules detected toward FG0.89SW in several transitions are presented in Fig.4, and the resulting measurements of rotation temperatures and column densities are listed in Table 4. These rotation temperatures are plotted in Fig.5 as a function of the molecular dipole moment. The results for column densities toward FG0.89NE are given in Table 5.

Most of these species have high dipole moments, and consequently high critical densities (>10^5 cm^{-3}). For low density gas (~10^3 cm^{-3}), the population of the different energy levels is not efficiently thermalized by collisions, but is coupled with the ambient radiation field, which, in the absence of any other radiative excitation (UV or IR pumping), consists of CMB photons. In this case, rotation temperatures then nearly equal the CMB temperature, which is expected to be T_{CMB}=5.14 K at z=0.89, assuming a scaling proportional to $(1+z)$. The derived rotation temperatures are consistent with this value. A thorough excitation analysis is beyond the scope of this paper, as it would require a careful treatment of collisional rates and partners (H_2 and e^-) for each molecule. This will be the subject of a future paper, in which we will also study the excitation in FG0.89NE with new multi-transitions observations, in order to derive an accurate and robust measurement of the CMB temperature at z=0.89 through the two independent lines of sight.

As a first step to interpreting the observations, we produced a LTE synthetic spectrum resulting from the combination of absorption lines from the molecular species listed in Table 4. We assume a common rotation temperature T_{rot}=T_{CMB}=5.14 K for all species and for the sake of simplicity, the absorption profile is set to be Gaussian with a FWHM of 20 km s^{-1} centered at V=0 km s^{-1} for the SW absorption (some lines are slightly offset from these values, see Table 4 and §4.3) and at V=−147 km s^{-1} for the few species for which NE absorption is detected. The partition functions were calculated for T=5.14 K by performing a direct sum over all energy levels. Their values are given in Table 4. Following Eq.2, the only free parameter is then the column density of each species. A kinetic temperature of 50 K was adopted to take into account the K-ladder population of the symmetric-top molecule CH_3CN (see §B.14).

The resulting LTE spectrum, obtained with the LTE column densities listed in Table 4, is overlaid on top of the observed spectrum in Fig.A.1. Despite the simplicity of the model, it reproduces relatively well the observations.

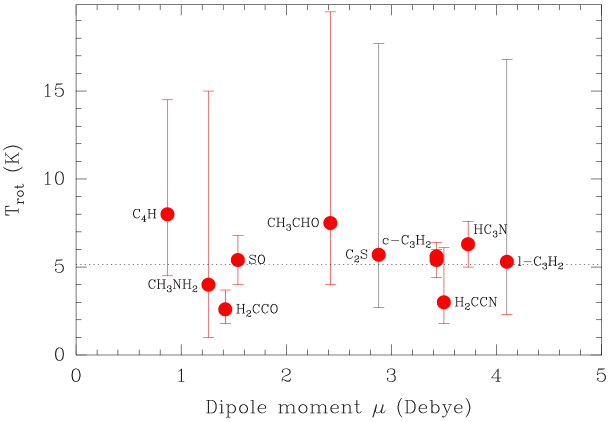

Fig. 5. Rotation temperatures as a function of molecular dipole moment. The dashed line indicates the value T_{CMB}=5.14 K at z=0.89, predicted from standard cosmology. Error bars indicate the 95% confidence interval.

In addition, we list in Table 6 the upper limits to the column densities and abundances obtained for some interstellar species of interest that have low-energy transitions within the frequency coverage of our survey. The upper limits to the integrated intensities were calculated as $3\sigma_\tau\sqrt{\delta V\Delta V_{1/2}}$, where σ_τ is the optical depth (Eq.1) noise level, δV is the velocity resolution, and $\Delta V_{1/2}$ the linewidth at half-maximum, which we fixed to 20 km s^{-1}. The upper limits to the column densities were calculated from Eq.2, again assuming LTE and T_{rot}=5.14 K.

3.5. Additional velocity components

Previous observations have shown that the molecular absorption profile consists of two main velocity components, separated by 147 km s^{-1} and located in front of the SW and NE images of the quasar (see Introduction). However, this picture should now be updated with the discovery of additional absorption components. Close to the redshifted frequencies of both the HCN and HCO$^+$ 1-0 lines (redshifted to ~47 and 47.3 GHz respectively) in Fig.A.1, several additional weak lines can be seen, which we failed to identify with other species. Those lines clearly arise at the same velocities for both HCN and HCO$^+$ 1-0 transitions, as shown in Fig.6. They therefore correspond to additional velocity components of HCN and HCO$^+$ 1-0 in the z=0.89 galaxy. The new components are located at −300, −224, −60, and +170 km s^{-1} (in addition to the previously known ones at 0 and −147 km s^{-1}). They probably arise in front of secondary continuum peaks along the Einstein ring (see for example Fig.3 by Chengalur et al. 1999). It would be interesting to determine their locations to constrain the kinematics of the galaxy, as well as their background continuum illumination to derive the associated opacities and column densities of gas along different sightlines through the disk. This is unfortunately impossible with the current data, which are limited in terms of angular resolution and sensitivity. Interestingly, the −300 and +170 km s^{-1} components have velocities beyond the range covered by HI absorption (Chengalur et al. 1999; Koopmans & de Bruyn 2005), and are nearly symmetrical with respect to the central velocity (~−80 km s^{-1} from the velocity of the SW absorption). These two components may arise from rapidly rotating gas near the center of the galaxy, e.g., in a circumnuclear ring.

Finally, we emphasize that we were unable to identify any lines originating from the second intervening galaxy at z=0.1926 (Lovell et al. 1996), neither from the host galaxy of the quasar at z=2.5 (Lidman et al. 1999), nor from Galactic absorption.

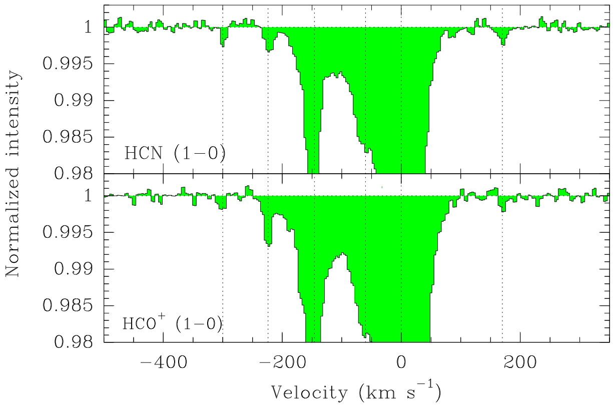

Fig. 6. Spectra of the HCO$^+$ and HCN 1-0 lines, showing the absorption components at 0 and −147 km s^{-1} (previously known, and arising toward the SW and NE images of the quasar, respectively), as well as the additional absorption components at velocities −300, −224, −60, and +170 km s^{-1}.

4. Discussion

The advantages of our survey are manifold. First, the 4-mm rest-frame window (redshifted to 7 mm at z=0.89), includes numerous ground state and low energy level transitions of a large range of intermediate-size interstellar molecules, and is therefore particularly interesting for an absorption study. Lighter molecules, e.g. hydrides, on the one hand, and heavier and more complex molecules (with ≥ 6 atoms) on the other hand, generally have these transitions at higher (mm/submm window) and lower (∼cm wavelengths) frequencies, respectively. The achieved sensitivity, of a fraction of a percent relative to the continuum intensity, and the large spectral coverage (20 GHz band) then allows us to detect many weak lines of rare molecules (i.e. with abundances of a few 10^{-11} relative to H_2) and in several cases, to build their rotation diagrams. For both runs (September 2009 and March 2010), observations were carried out within one or two days, i.e. a timescale shorter than the time delay of the lens (∼24 days, Lovell et al. 1998; Wiklind & Combes 1999) and much smaller than the timescale for variations in the absorption profiles, of the order of several months (Muller & Guélin 2008). The comparison of lines in the frequency overlap between the two datasets shows that the relative variations between September 2009 and March 2010 are smaller than ∼5% for the strong HCO$^+$/HCN 1-0 lines and yet smaller for other lines. Time variations are therefore negligible, and moreover, would affect only the few lines in the small frequency overlap between both observing runs. Finally, the absorption technique provides a high spatial resolution, equivalent to the angular size of the quasar continuum images and corresponding to a few parsecs in the plane of FG0.89.

On the other hand, several limitations have to be kept in mind. First, the detection of molecular species in our survey (for a given abundance) is obviously biased towards those that have *i)* a relatively high dipole moment, *ii)* a relatively low partition function, and *iii)* low energy transitions within the frequency coverage (57–94 GHz, rest-frame). The molecular inventory is then limited by a combination of these properties. Second, the angular resolution of our observations is insufficient to resolve the background continuum emission. While the different absorption components are well-resolved kinematically, this introduces an uncertainty in the continuum illumination, hence also in the line opacities and column densities. We argue however that the associated uncertainties are only ∼10% for the bulk of the lines (see §.3.3). Moreover, the spectral resolution is only a factor of a few smaller than the width of the line (∼20 km s^{-1}). This reduces the absorption line depths, likely causing opacities to be slightly underestimated. We expect that this affects weak lines the most. The limited spectral resolution also prevents us from measuring the saturation level of the HCO$^+$/HCN 1−0 SW lines, which could help us to derive the NE/SW flux ratio. Finally, we assume a source covering factor of unity for each absorption component, implying that the derived optical depths and column densities are, strictly speaking, lower limits.

4.1. Isotopic ratios

Isotopic abundances are directly affected by nucleosynthesis processes in stellar interiors, and isotopic ratios are thus good probes of the chemical enrichment history of the Universe. For this purpose, molecular absorption offers interesting prospects, owing to the rotational transitions of different isotopologues being easily resolved at mm wavelengths, such that low column densities of the rare isotopologues are still detectable e.g. for most isotopes of C, N, O, and S elements, and that abundances can be inferred directly from absorption optical depths (if the line of the most abundant isotopologue is not saturated).

The ^{12}C/^{13}C, ^{14}N/^{15}N, ^{16}O/^{18}O, ^{18}O/^{17}O, and ^{32}S/^{34}S isotopic ratios were derived in FG0.89SW by Muller et al. (2006), based on observations of the different isotopologues of HCO$^+$, HCN, HNC, CS, and H_2S at 3 mm with the Plateau de Bure interferometer. These ratios, particularly ^{18}O/^{17}O and ^{32}S/^{34}S, reveal significant differences when compared to sources in the Local Universe (see Table 7 from Muller et al. 2006). Interestingly, comparable values are found using the same absorption technique in the z=0.68 galaxy located in front of the quasar B 0218+357 (Muller et al. in prep.). These results are essentially consistent with the expectation that low-mass stars (<1.5 M$_\odot$) had no (or only a short) time to play a major role in the gas enrichment of such young (a few Gyr old) galaxies.

Our 7 mm survey now allows us to check the previous results obtained at 3 mm in FG0.89SW, in particular for lines with different optical depths. In addition, time variability is not a concern for this 7 mm dataset. Unfortunately, the limited spectral resolution of the survey prevents us from measuring ratios across the lines, which is a thorough test of possible saturation, and we simply derive the isotopic ratios from the ratios of integrated opacities.

The spectra of different isotopologues of HCO^+, HCN, HNC, and SiO as observed in our 7 mm survey are shown in Fig.7. Results for the corresponding isotopologue abundance ratios are given in Table 7, where we also report the ratios previously measured at 3 mm. Our final estimates for the various isotopic ratios in FG0.89SW are given in Table 8. The values obtained from 7 mm and 3 mm data are in very good agreement. We hereafter discuss how we derived those ratios.

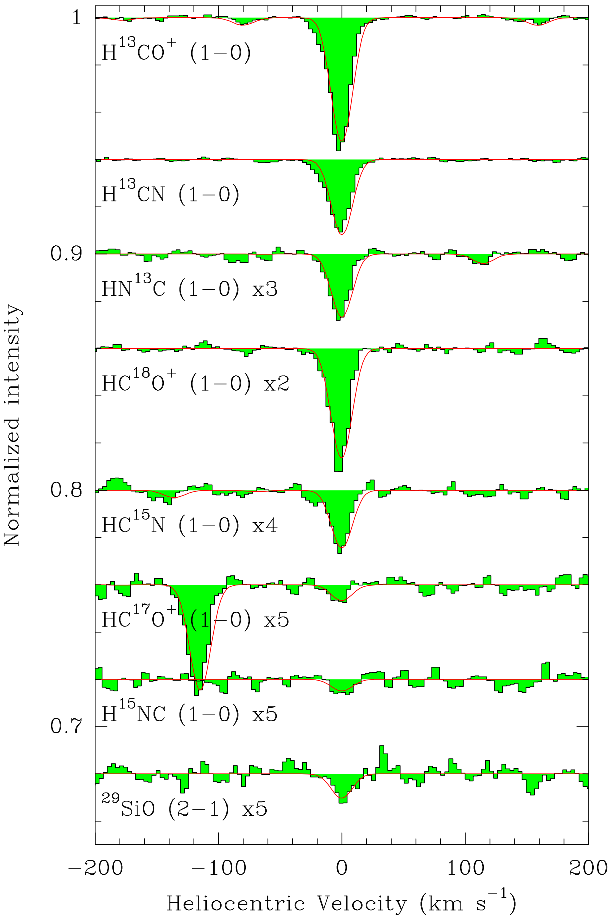

Fig. 7. Spectra of the different isotopologues of HCO^+, HCN, HNC, and SiO.

4.1.1. Deuterium

We do not detect lines from any of the deuterated species DCO^+/DCN, down to levels of a few 10^{-4}, which is higher than the D/H cosmic abundance of 2.5×10^{-5} (e.g. Spergel et al. 2003). This is consistent with no strong fractionation enhancement, as expected in a relatively warm gas component (T_{kin}~50 K) with a moderate density, $n(H_2)$ of the order of a few 10^3 cm^{-2}.

4.1.2. Carbon

It is not straightforward to go from the abundance ratio $^{12}C\star/^{13}C\star$, where $C\star$ is a given carbon-bearing molecule, to a value of the $^{12}C/^{13}C$ isotopic ratio, because the measured abundance ratio can be affected by opacity effects, chemical fractionation and/or selective photodissociation. Hence, observations of several ^{12}C- and ^{13}C- bearing molecules are highly desirable.

The interstellar gas phase abundance of ^{13}CO and $^{13}C^+$ relative to CO and C^+, can be affected by the isotopic fractionation reaction

$$^{13}C^+ + CO \longleftrightarrow {}^{13}CO + C^+ + 35\ K. \tag{4}$$

In cold molecular clouds, ^{13}C then becomes mostly trapped in ^{13}CO, and the abundance of the $^{13}C^+$ ion decreases. The $^{12}C\star/^{13}C\star$ ratio for species formed from CO should thus reflect the $^{12}C/^{13}C$ isotopic ratio, while for others $^{12}C\star/^{13}C\star > {}^{12}C/^{13}C$ should be observed. This was first investigated by Langer et al. (1984) for various carbon-bearing species. They found that the $^{12}C/^{13}C$ isotopic ratio should be within the limits set by the $^{12}CO/^{13}CO$ and $H_2^{12}CO/H_2^{13}CO$ ratios. Since HCO^+ can be produced from both CO and other species, it can be enhanced in either ^{12}C or ^{13}C, depending on the physical conditions.

The $^{12}C\star/^{13}C\star$ abundance ratios are listed in Table 7 for relevant species. The $HCO^+/H^{13}CO^+$ ratio might be underestimated because of the large opacity of the ^{12}C isotopologue. The opacity of HNC, on the other hand, is lower, and the $HNC/H^{13}NC$ abundance ratio might more accurately reflect the $^{12}C/^{13}C$ elemental ratio. We do not detect transitions from either the ^{13}CCH or $C^{13}CH$ isotopomers, which implies that the lower limits to the abundance ratios are $C_2H/^{13}CCH>58$ and $C_2H/C^{13}CH>43$. Sakai et al. (2010) found ^{13}C abundance anomalies in the ^{13}C-isotopomer of C_2H toward TMC 1 and L1527, with the ^{13}C-species underabundant relative to the interstellar $^{12}C/^{13}C$ ratio. In addition, the two carbon atoms do not appear to be equivalent in the formation pathways of the molecule, as Sakai et al. (2010) measured an abundance ratio $C^{13}CH/^{13}CCH = 1.6$ toward both sources. They conclude that carbon-chain molecules are not indicated to determine the $^{12}C/^{13}C$ elemental ratio, because of the positional differences and heavy ^{13}C dilution. The non-detection of $H_2^{13}CO$ points to a ratio $H_2CO/H_2^{13}CO>173$, suggesting that fractionation could affect our estimate of the $^{12}C/^{13}C$ isotopic ratio. On the basis of all these results, we choose to adopt the average ratio $^{12}C/^{13}C=35 \pm 11$, obtained from the HCO^+, HCN, and HNC species.

This value of $^{12}C/^{13}C$ is less than half the ratio measured in the Solar System (89, Lodders 2003), but closer to that derived in the local interstellar medium (59 ± 2, Lucas & Liszt 1998) and especially close to that in the starburst galaxies NGC253 and NGC4945 (40–50, Henkel et al. 1993; Curran et al. 2001; Wang et al. 2004). It is, however, much lower than the value that would be expected in a poorly processed environment (e.g. Kobayashi et al. 2011). We note that Martín et al. (2010) used C_2H and CO isotopologues to revisit the $^{12}C/^{13}C$ ratios in NGC253 and M82 and found values larger than the ratios measured in previous studies. The interstellar $^{12}C/^{13}C$ isotopic ratio clearly remains difficult to determine.

Toward the NE component, we do detect neither the $H^{13}CO^+$ nor the $H^{13}CN$ 1-0 absorptions, with lower limits $HCO^+/H^{13}CO^+>71$ and $HCN/H^{13}CN>41$ (at 3 σ level), respectively. As the NE absorption is located at an even larger galactocentric distance than the SW, thus in a region likely to be even less processed, we expect a $^{12}C/^{13}C$ ratio larger than that toward FG0.89SW.

4.1.3. Nitrogen

There are two ways of estimating the ^{14}N/^{15}N isotopic ratios from our data: either from the direct HCN/HC^{15}N and HNC/H^{15}NC abundance ratios, or, indirectly from the H^{13}CN/HC^{15}N and HN^{13}C/H^{15}NC ratios, after correcting for the ^{12}C/^{13}C isotopic ratio.

We obtain the ratios HCN/HC^{15}N=192 ± 11, and HNC/H^{15}NC=340 $^{+120}_{-70}$. The former ratio might be underestimated because of opacity effects on the HCN line, but the second ratio has a large uncertainty. Using the ^{13}C variants, we obtain H^{13}CN/HC^{15}N=5.3 ± 0.3 and HN^{13}C/H^{15}NC=7.3$^{2.5}_{-1.5}$. The use of a large ^{12}C/^{13}C ratio (>50) gives a ^{14}N/^{15}N ratio close to the value observed in the local interstellar medium (=237 $^{+27}_{-21}$, Lucas & Liszt 1998) and in the Solar System (=272, Lodders 2003). Using our estimate ^{12}C/^{13}C=35 ± 11 and the ratio H^{13}CN/HC^{15}N=5.3 ± 0.3, we derive ^{14}N/^{15}N=190 ± 60.

Whether this value actually reflects the true ^{14}N/^{15}N isotopic ratio is however uncertain if fractionation is an issue for nitrogen-bearing species (Rodgers & Charnley 2008a,b). The recent measurements of Lis et al. (2010) toward the two cold dense molecular clouds Barnard 1 and NGC1333 do not suggest a high ^{15}N enhancement.

We note that the ^{15}N isotopologues of N_2H^+ are not detected, implying formally that ^{14}N/^{15}N > 90.

4.1.4. Oxygen

As for ^{14}N/^{15}N, the ^{16}O/^{18}O isotopic ratio can be estimated either directly from the HCO$^+$/HC^{18}O$^+$ abundance ratio, or indirectly from H^{13}CO$^+$/HC^{18}O$^+$. The former method yields a ratio ^{16}O/^{18}O=50 ± 1, while the latter implies that ^{16}O/^{18}=80 ± 25. Even considering that our value of ^{12}C/^{13}C could be underestimated, the ^{16}O/^{18}O isotopic ratio derived in FG0.89SW is much lower than that in both the local interstellar medium (=672 ± 110, Lucas & Liszt 1998) and the Solar System (=499, Lodders 2003), in likely connection with the youth of the galaxy.

Remarkably, the ^{18}O/^{17}O isotopic ratio, measured directly from the H^{18}CO$^+$ and HC^{17}O$^+$ J=1-0 optically thin lines, also differs significantly from values for sources in the Local Universe (< 6, see e.g. Table 7 of Muller et al. 2006). While a value of ^{18}O/^{17}O=12 $^{+2}_{-3}$ was measured from the J=2-1 lines, the marginal detection of HC^{17}O$^+$ at 7 mm (Fig.7) yields H^{18}CO$^+$/HC^{17}O$^+$=20 $^{+7}_{-4}$. This new estimate of the ^{18}O/^{17}O isotopic ratio confirms the large value previously obtained from the J=2-1 lines at 3 mm.

4.1.5. Silicon

The detection of the ^{28}SiO and ^{29}SiO J=2-1 line allows us to estimate the isotopic ratio ^{28}Si/^{29}Si=11 $^{+4}_{-2}$. Both SiO lines are optically thin, unless the source covering factor is much lower than unity. This ^{28}Si/^{29}Si ratio at z=0.89 is nearly half the value measured in the Solar System, 19.6 (Lodders 2003).

The situation is similar to that for the ^{32}S/^{34}S isotopic ratio, estimated to be 10.5 ± 0.6 from the CS/C^{34}S and H$_2$S/H$_2^{34}$S abundance ratios in FG0.89SW (Muller et al. 2006), whereas it is 22 in the Solar System. Interestingly, the magnesium isotopic ratios were derived from UV-spectroscopy for a z=0.45 absorption line system (Agafonova et al. 2011), and also suggest that there is a significant relative overabundance of heavy Mg isotopes. Silicon and sulfur (and magnesium) are both produced by massive stars. That the neutron-enriched isotopes appear to be more abundant at z=0.89 than in the Local Universe might provide some constraint on their nucleosynthesis.

Table 7. Isotopologues abundance ratios toward FG0.89SW.

Abundance ratios	@7 mm	@3 mm
DCO$^+$/HCO$^+$	$< 7.1 \times 10^{-4}$	–
DCN/HCN	$< 8.4 \times 10^{-4}$	–
DNC/HNC	–	< 0.015
DCO$^+$/H^{13}CO$^+$	< 0.015	–
DCN/H^{13}CN	< 0.030	–
HCO$^+$/H^{13}CO$^+$	21.2 ± 0.2	28 ± 3
HCN/H^{13}CN	36.3 ± 0.5	$40\ ^{+7}_{-5}$
HNC/HN^{13}C	47 ± 2	27 ± 3
H$_2$CO/H$_2^{13}$CO	> 173 (3σ)	–
C$_2$H/^{13}CCH	> 58 (3σ)	–
C$_2$H/C^{13}CH	> 43 (3σ)	–
HCN/HC^{15}N	192 ± 11	–
HNC/H^{15}NC	$340\ ^{+120}_{-70}$	$166\ ^{+194}_{-58}$
H^{13}CN/HC^{15}N	5.3 ± 0.3	4.2 ± 0.3
HN^{13}C/H^{15}NC	$7.3\ ^{+2.5}_{-1.5}$	$6\ ^{+4}_{-2}$
HCO$^+$/HC^{18}O$^+$	48 ± 1	$53\ ^{+16}_{-10}$
H^{13}CO$^+$/HC^{18}O$^+$	2.29 ± 0.05	2.01 ± 0.07
HC^{18}O$^+$/HC^{17}O$^+$	$19.6\ ^{+7}_{-4}$	$12\ ^{+3}_{-2}$
^{28}SiO/^{29}SiO	$11\ ^{+4}_{-2}$	–

Table 8. Isotopic ratios toward FG0.89SW.

Isotopic ratios	7 mm	3 mm	Averaged
D/H	$< 7 \times 10^{-4}$	< 0.015	–
^{12}C/^{13}C	35 ± 11	32 ± 6	33 ± 5
^{14}N/^{15}N	190 ± 60	143 ± 30	152 ± 27
^{16}O/^{18}O	80 ± 25	66 ± 12	69 ± 11
^{18}O/^{17}O	$20\ ^{+7}_{-4}$	$12\ ^{+3}_{-2}$	$13\ ^{+3}_{-2}$
^{32}S/^{34}S	–	10.5 ± 0.6	10.5 ± 0.6
^{28}Si/^{29}Si	11^{+4}_{-2}	–	11^{+4}_{-2}

Notes. The values at 3 mm were rederived from Muller et al. (2006) data using the same methodology as described in the text.

4.2. Comparative chemistry

It is interesting to compare the molecular abundances in the z=0.89 galaxy with those measured for various sources in the Local Universe, to characterize the type of clouds and chemistry. For this purpose, we selected a sample of archetype sources with a large number of detected molecular species, usually covered by large spectral surveys. Molecular abundances in circumstellar envelopes around evolved stars, such as IRC+10216, were not included because of the distinctive chemical segregation within the envelope. We preferred to use data obtained from a single team/telescope, for the sake of homogeneity and to minimize beam effects.

Despite the low density and poor shielding from the interstellar radiation field, a variety of molecules is already present in Galactic diffuse clouds ($A_V < 1$): about 15 different species have been detected so far (see e.g. Liszt et al. 2008), and the limit of their chemical complexity remains unclear. We mention here that column densities in diffuse clouds are most often determined through mm-wave absorption toward extragalactic continuum sources, similar to the work presented in this paper.

Translucent clouds ($2<A_V<5$) are expected to have a richer chemistry, with about 30 molecules detected so far, including highly unsaturated and very reactive hydrocarbon chains. We adopt the molecular abundances compiled by Turner (2000).

Cold dark clouds are the sites of low-mass star formation, where an intricate gas-phase ion-molecule interstellar chemistry takes place. We adopt the abundances determined by Ohishi et al. (1992) toward TMC-1, which is a prototype of dark clouds.

Hot and dense cores, associated with massive-star formation harbor the most complex interstellar chemistry. There, the chemistry is characterized by the evaporation of dust grains, releasing large molecules in the gas phase. We adopt the abundances derived by Nummelin et al. (2000) in the region Sgr B2N toward the Galactic center as reference.

Finally, we also include in our comparison three extragalactic sources for which molecular abundances have been derived for a significantly large number of species: the nuclear regions of the starburst galaxies NGC253 and NGC4945 (Martín et al. 2006 and Wang et al. 2004, respectively), as well as the star forming region N113 in the Large Magellanic Cloud (LMC, Wang et al. 2009).

The comparison of abundances derived in FG0.89SW with those observed toward these various sources is illustrated in Fig.8. Molecular abundance ratios, normalized to FG0.89SW and detailed by species, are also given in Fig.9. Several species in our survey, such as HCO^+, HCN, C_2H, and c-C_3H_2 are commonly observed in Galactic diffuse clouds. More complex molecules (e.g. carbon chains) are only seen toward cold dark clouds or in warm and dense clouds.

Comparing molecular abundances relies on the validity of various hypotheses. First, molecules have to be co-spatial and share the same source covering factor. The size of the SW and NE compact continuum components corresponds to a few pc in the plane of the z=0.89 galaxy. We assume a common source covering factor of unity for all molecules. However, the absorbing gas could be the mix of (most likely several) dense cores embedded in a more diffuse component within the continuum beam illumination. Our derived column densities and molecular abundances are thus lower limits. In addition, opacity effects, if not correctly taken into account, could easily lead to erroneous molecular abundances. For this reason, we do not use the abundances of HCO^+, HCN, and C_2H from Nummelin et al. (2000) toward Sgr B2N, as they are probably largely underestimated. Finally, a reference species needs to be assigned for normalization, in order to compare the relative molecular abundances. We choose to normalize the column densities to that of molecular hydrogen, as commonly done in the literature. For this, we assume a value $N(H_2)=2 \times 10^{22}$ cm^{-2} toward the SW component, as estimated by Wiklind & Combes (1998). This value is consistent with the measurement of $N(H)=(3.5 \pm 0.6)\times10^{22}$ cm^{-2} obtained from X-ray absorption by Mathur & Nair (1997) assuming that all absorption is due to the SW component. The absorbing gas is indeed mostly molecular along this line of sight (Chengalur et al. 1999), so that $N(H_2)$ should be close to $2\times N(H)$. The NE line of sight, on the other hand, intercepts the disk of the z=0.89 galaxy at a galactocentric distance of ∼4 kpc. There, the extinction A_V is roughly one order of magnitude lower than toward the SW image of the quasar (e.g. Falco et al. 1999, see also Fig.1), and the column density of molecular gas is likely to be similarly lower. We assume a H_2 column density of 1×10^{21} cm^{-2} toward FG0.89NE. This choice makes the fractional abundances similar to those in Galactic diffuse clouds (Table 9 and Fig.9). While the normalization to H_2 introduces an uncertainty in the absolute molecular abundances, abundance ratios for a given source are not affected, and should therefore bear greater significance (again provided that the species are co-spatial and have an identical source covering factor).

To compare the overall trend between the various sources, and inspired by Martín et al. (2006), we have calculated an abundance estimator χ_{ij}, defined as the average of the logarithm of abundance ratios between two sources i and j

$$\chi_{ij} = \frac{1}{N_{mol}} \sum_{k=1}^{N_{mol}} \log_{10} \left(\frac{X_{i,k}}{X_{j,k}} \right), \quad (5)$$

where $X_{i,k}$ stands for the abundance relative to H_2 of molecule k in source i, and the sum runs over all N_{mol} molecules detected in common for the two sources i and j. A dispersion in the estimator was also calculated to reflect potential large variations in the abundance ratios between species. We do not take into account non-detections in this estimator. Abundance estimators were also calculated in the same manner for the following sub-samples of molecules: carbon chains (i.e. with more than two chained carbon atoms, such as l-C_3H, C_4H, c-C_3H_2, l-C_3H_2, and HC_3N), sulfur-bearing species (i.e. SO, NS, H_2CS, C_2S, and SO^+), and saturated molecules (CH_3OH and CH_3NH_2), presumably all formed on dust grains. The value of χ_{ij} was calculated between FG0.89SW and the other sources only if the number of common species for two objects was $\geq$2. The abundance estimators are given in Table 10 and illustrated in Fig.10.

On the basis of the abundance estimators including all species, we obtain a basic sequence of increasing molecular abundances such as LMC < diffuse clouds < FG0.89NE < NGC253 < FG0.89SW < NGC4945 < TMC 1 < translucent clouds < Sgr B2N, indicating, unsurprisingly, that the chemical abundances in FG0.89SW are in-between those in typical Galactic diffuse and translucent clouds.

The dispersions for Sgr B2N are large, though it is clear that sulfur-bearing and especially saturated species have much higher abundances in this molecular-rich object. In TMC 1 and translucent clouds, the abundance of carbon chains is globally a factor of a few higher than in FG0.89SW, while that of sulfur-bearing species is one order of magnitude higher.

The overall similarity between the molecular abundances of FG0.89SW and the nuclear region of the starburst galaxy NGC253 is surprising. Martín et al. (2006)

found good agreement between the molecular abundances in NGC253 and those at the position Sgr B2(OH) in the Galactic center molecular cloud Sgr B2. Shocks are thought to play an important role in the heating and chemistry toward these nuclear clouds, triggering the disruption of dust grains, and releasing the products of grain-surface chemistry into the gas phase. It is tempting to invoke similar chemical processes in FG0.89SW, as they could explain all of the similarities between the molecular abundances, the high kinetic temperature of the gas, and the relatively large linewidth (see also discussions in Henkel et al. 2008; Menten et al. 2008). Moreover, the elemental composition of the gas in both galaxies is expected to be dominated by the nucleosynthesis products of massive stars, because of their shorter timescales. The major difference, though, is that FG0.89SW clouds are located in a spiral arm at a galactocentric distance of about 2 kpc, and gas densities are likely lower. Abundances in NGC4945 show some differences, albeit small, when compared to those in NGC253. They are interpreted as different starburst evolutionary states (Wang et al. 2004; Martín et al. 2006). The systematically lower molecular abundances in the LMC-N113 region are attributed to a photon dominated region (PDR) in a nitrogen deficient environment (Wang et al. 2009). Nevertheless, we emphasize that, because of the limited angular resolution of these extragalactic observations, the corresponding molecular abundances reflect the average of the different types of cloud gas properties and excitation conditions within the beam. This is much less the case for absorption line studies toward quasars, where the spatial resolution is set by the small size of the background continuum emission.

It will be interesting to investigate the chemical complexity toward FG0.89SW when searching for more species, especially light hydrides and larger molecules. The molecular absorber located at z=0.68 in front of the quasar B 0218+357 would also be a suitable target for these investigations.

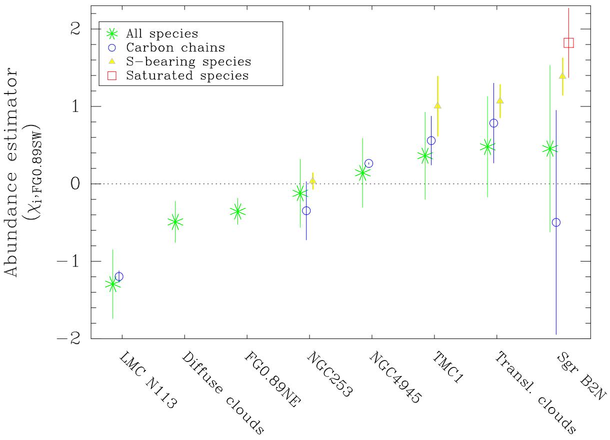

Fig. 10. Comparison of the abundance estimators χ_{ij} as defined in Eq.5, for different sources and sub-samples of molecular species (see text), with respect to FG0.89SW.

4.3. Kinematics

4.3.1. Velocity centroids and line profiles

The limited velocity resolution of our survey (6–10 km s^{-1}, although slightly improved after the Doppler correction) prevents us from conducting a detailed analysis of the kinematics and line profiles. Nevertheless, the high S/N of most of the lines allows us to determine the velocity centroids of a large number of species from Gaussian fitting, with an uncertainty of the order of one km s^{-1} or better. Inter-species velocity offsets can then be tested statistically. The results are shown in Fig.11, where we show the FWHM versus the velocity centroid derived from Gaussian fits for species seen toward the SW absorption.

Excluding the strong and likely saturated absorption of HCO^+ and HCN, we obtain an average velocity of -1.78 ± 1.83 km s^{-1} toward FG0.89SW. Few species, namely CH_3NH_2, CH_3OH, l-C_3H, HNCO, SO^+, and HC_3N, have velocities that differ from this average by more than 1 σ. These kinematical differences might be due, e.g., to chemical segregation along the line of sight, different source covering factors per species, excitation conditions, asymmetric line profiles, or a limited velocity resolution and/or S/N of the observations. Another interpretation is explored in the next section. After removing the outliers listed above, we obtain a new estimate of the average velocity: -1.51 ± 0.73 km s^{-1}, the dispersion dropping by a factor of more than two with respect to the first value including outliers.

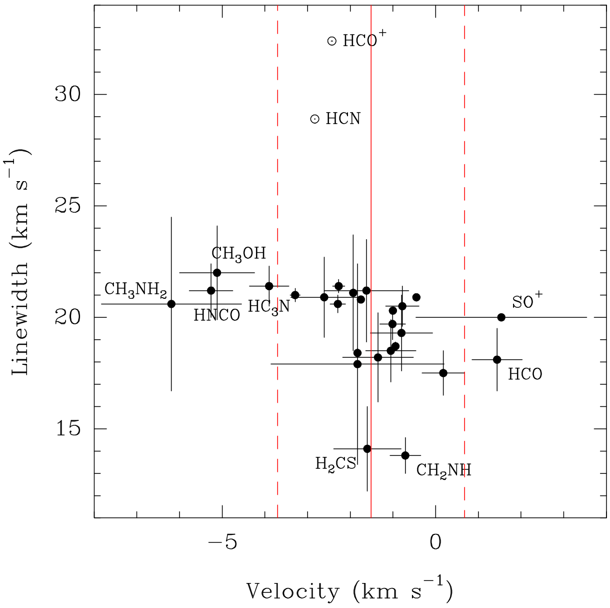

Fig. 11. Diagram of the FWHM versus velocity centroids, derived from Gaussian fits to the lines toward FG0.89SW. The average velocity (*full line*) and 3σ dispersion (*dashed lines*), calculated from 22 species (see text), are indicated. The two points with a linewidth larger than 25 km s^{-1} correspond to HCO^+ and HCN, the lines of which are likely saturated.

4.3.2. Constraints on the variation in the fundamental constants

We now discuss the interpretation of the velocity offsets in terms of variations in the fundamental constants of physics, and more particularly, in the proton-to-electron mass ratio.

Searches for observational evidence of any secular variation in the fundamental constants (FC) of physics has attracted much attention lately. Any discovery of such evidence would indeed contradict the Standard Model in the invariance principle, and open new horizons in physics research. We note that several theories predict that the fundamental constants vary, and we refer the interested reader to a review of this field by Uzan (2011). A description of the various methods that have been applied to constrain the variation in the fundamental constants to date, their results, and potential systematics are also given in this review.

Spectroscopic observations of absorption lines toward high-redshift quasars naturally offer very long time lapse, possibly longer e.g. than the age of the Solar System, that could allow even small variation rates to be measured. While different methods have been developed, they all consist of a change in the frequency of atomic or molecular transitions induced by a potential variation of the (dimensionless) fine structure constant (α), proton-to-electron mass ratio (μ=m_p/m_e), and nuclear g-factor (g_n). One can write this change as

$$\frac{\Delta\nu}{\nu} = K_\alpha\frac{\Delta\alpha}{\alpha} + K_\mu\frac{\Delta\mu}{\mu} + K_g\frac{\Delta g_n}{g_n} = \sum_{C=\alpha,\mu,g_n} K_C\frac{\Delta C}{C}, \quad (6)$$

where the K_i coefficients reflect the sensitivity of a change in the frequency of the transition ν to a change in the constant C=α, μ and/or g_n. The comparison of two different lines is then given by

$$\frac{\Delta V}{c} = \frac{V_i - V_j}{c} = \sum_{C=\alpha,\mu,g_n}(K_{C,j} - K_{C,i})\frac{\Delta C}{C}, \quad (7)$$

where ΔV is the velocity difference between the lines i and j induced by changes in FCs. From Eq.7, it is clear that only the comparison of lines with different K_C sensitivity coefficients yields a possibly non-null velocity shift. For example, one has $|K_\alpha|$<<1, K_μ=$-$1 and $|K_g|$<<1 for rotational transitions. For hyperfine transitions, K_α=$-$2, K_μ=$-$1, and K_g=$-$1. Therefore, the comparison of hyperfine and rotational lines is sensitive to a variation of $\Delta F/F$, where F=$\alpha^2 g_n$.

Inversion lines of ammonia have a high sensitivity to any variation in μ, with K_μ=$-$4.46, but are nearly insensitive to changes in other constants (Flambaum & Kozlov 2007). As a result, the comparison of NH_3 inversion lines and other rotational transitions provide a test of $\frac{\Delta\mu}{\mu}$. This method was used toward the quasars B 0218+357 and PKS 1830$-$211 (the only two known high-z ammonia absorbers) and yields no significant evidence of changes in μ, with constraints on $\frac{\Delta\mu}{\mu}$ down to a few 10^{-7} (Murphy et al. 2008; Henkel et al. 2009; Kanekar 2011), corresponding to a velocity offset of the order of a few tenths of km s^{-1}. Nevertheless, the method is limited by the following systematic effects: (1) local velocity offsets between species; (2) non-LTE and saturation effects for NH_3 hyperfine strucure (if hyperfine components are unresolved or poorly detected) and optically thick lines, respectively; (3) time variations (if observations are taken at different epochs); and (4) changes in the continuum morphology at significantly different frequencies.

Henkel et al. (2009) measured a velocity of -3.70 ± 0.43 km s^{-1} for HC_3N, consistent with our value of -3.90 ± 0.46 km s^{-1}. They used this value as a reference to constrain the velocity shift of NH_3 inversion transitions, obtaining a 3 σ upper limit on $\frac{\Delta\mu}{\mu}$ of 1.4×10^{-6}. Taking our average velocity (without outliers) as reference instead, we derive a new value $\frac{\Delta\mu}{\mu}$=$(-2.04 \pm 0.74)\times10^{-6}$ from the ammonia velocity shift, assuming no time variations between the different observations and that the shift is indeed due to variations in μ. Taken at face value, the velocity dispersion of the different species in our survey introduces a significant contribution as *kinematical noise*, potentially limiting constraints on $\frac{\Delta\mu}{\mu}$ to $\sim2\times10^{-6}$ using inversion lines of ammonia.

Interestingly, methanol was also found to have transitions with high sensitivity to change in the proton-to-electron mass ratio (Jansen et al. 2011). The crude offset between the velocity of methanol and the average velocity is ΔV=-3.75 ± 0.89 km s^{-1}. Taking the sensitivity coefficient K_μ=-7.4 for the methanol transition at 60.531477 GHz (Jansen et al. 2011) and provided that the velocity offset is due only to a variation in μ, we obtain $\frac{\Delta\mu}{\mu}$=$(-1.95 \pm 0.47)\times10^{-6}$, that is, a statistical 4 σ significant detection of a variation in μ at z=0.88582[5], in agreement with the ammonia result. However, since we detect only one methanol line in our survey, we consider this result as only tentative. More conservatively, our observations give an upper limit $|\frac{\Delta\mu}{\mu}|<4\times10^{-6}$, which, importantly, takes into account the velocity dispersion of a large number of molecular species. More species and lines with different sensitivity coefficients should be observed at high velocity resolution and high S/N to check the compatibility with variations in μ. We note that Kanekar (2011) derived $\frac{\Delta\mu}{\mu}$=$(-3.5 \pm 1.2)\times10^{-7}$ at z=0.68 from the comparison of NH_3 inversion lines and rotational lines of two species, CS and H_2CO, seen in absorption toward B 0218+357.

5. Summary and conclusions

We have completed the first unbiased spectral survey toward an intermediate-redshift molecular absorber, the z=0.89 galaxy located in front of the quasar PKS 1830$-$211. Observations, performed with the Australian Telescope Compact Array, cover the 7 mm band from 30 to 50 GHz (equivalent to the rest-frame frequency interval 57–94 GHz), and reach a sensitivity of the order of a few times 10^{-3} of the continuum level, at a spectral resolution of 1 MHz.

The brightness of the background quasar, the large column density of absorbing molecular gas, the large instantaneous instrumental bandwidth, the wide frequency coverage of our survey, and the frequency band most sensitive to low energy transitions of numerous molecules, all concur in allowing us to achieve the first large chemical inventory in the interstellar medium of a distant galaxy.

From these observations, we derive the following results:

---

[5] That is, a look-back time of 7.24 Gyr for H_0=71 km s^{-1} Mpc^{-1}, Ω_M=0.27, and Ω_Λ=0.73.

- We detect a total of 28 molecular species toward the SW image of the quasar (of which more than half are detected for the first time toward this target and eight are detected for the first time outside the Milky Way: SO^+, l-C_3H, l-C_3H_2, H_2CCN, H_2CCO, C_4H, CH_3NH_2, and CH_3CHO), and six toward the NE image.
- The rotation temperatures are close to the expected cosmic microwave background temperature, 5.14 K, at z=0.89. This absorber, with strong absorption along two independent lines of sight, offers a unique opportunity to establish a robust and accurate measurement of T_{CMB} at z=0.89.
- The fractional molecular abundances toward the SW absorption are found to be in-between those in typical Galactic diffuse and translucent clouds.
- Toward the NE absorption, where the column density of molecular gas is about one order of magnitude lower, the fractional abundances are comparable with those in diffuse clouds.
- The isotopic ratios of C, N, O, and Si at 7 mm confirm and complement the C, N, O, and S ratios previously obtained by Muller et al. (2006) at 3 mm. Significant differences are found from the solar and local ISM values, which could be explained by the limited timescale for nucleosynthetic processing at z=0.89. Deuterated species remain undetected down to a D/H ratio of $<7\times10^{-4}$.
- We discover several new, but weak, velocity components, at V=−60, −224, and −300 km s^{-1}, seen in the HCO^+ and HCN (1-0) lines.
- The analysis of the velocity centroids yields a dispersion of nearly 2 km s^{-1} toward FG0.89SW. Among the species showing a significant offset from the average velocity, NH_3 (observed by Henkel et al. 2009) and CH_3OH both have a high sensitivity to variations in the proton-to-electron mass ratio μ. We derive a conservative upper limit of $|\frac{\Delta\mu}{\mu}|<4\times10^{-6}$ at z=0.89, which includes the velocity dispersion (hence the uncertainty caused by potentially different spatial distributions) of a large number of molecular species. Further observations of lines with different sensitivity coefficients will be required to place stronger constraints on variations in μ.

The new generation of instruments currently deployed (ALMA, EVLA, NOEMA) will offer new capabilities in terms of frequency coverage, instantaneous bandwidth, sensitivity, and spectral resolution that will be of great benefit to molecular absorption studies. It will be interesting to investigate the chemistry and its complexity in this distant z=0.89 galaxy, as well as toward other known molecular absorbers.

Acknowledgements. We wish to thank Phil Edwards for his help and to acknowledge additional Director's observing time allocated in March 2010 to complete the project. We are grateful to Jamie Stevens and Kate Randall for their help with observations. We thank the referee, Rainer Mauersberger, and the editor, Malcolm Walmsley, for their comments on the manuscript, and Claire Halliday for the language editing. We thank Sergei Levshakov for pointing out a mistake in the upper limit to the μ variation in a previous version of the manuscript. This research has made intensive use of the Cologne Database for Molecular Spectroscopy and Jet Propulsion Laboratory Molecular Database. The Australia Telescope Compact Array is part of the Australia Telescope which is funded by the Commonwealth of Australia for operation as a National Facility managed by CSIRO. S.M. acknowledges the support of a NORDFORSK grant in 2009–2010.

References

Agafonova, I. I., Molaro, P., Levshakov, S. A. & Hou, J. L., 2011, A&A, 529, 28
Agúndez, M., Fonfría, J. P., Cernicharo, J., Pardo, J. R. & Gu'elin, M., 2008, A&A, 479, 493
Apponi, A. J. & Ziurys, L. M., 1997, ApJ, 481, 800
Apponi, A. J., Pesch, T. C. & Ziurys, L. M., 1999, ApJ, 519, L89
Ball, J. A., Gottlieb, C. A., Lilley, A. E. & Radford, H. E., 1970, ApJ, 162, L203
Ball, J. A., Gottlieb, C. A., Lilley, A. E. & Radford, H. E., 1971, IAU Circ., No.2350
Bottinelli, S., Hughes, A. M., van Dishoeck, E. F., et al., 2009, ApJ, 690, L130
Cernicharo, J., Gottlieb, C. A., Guélin, M., et al., 1991, ApJ, 368, L39
Cernicharo, J., Cox, P., Fossé D. & Güsten, R., 1999, A&A, 351, 341
Cernicharo, J., Guélin, M. & Kahane, C., 2000, A&AS, 142, 181
Chengalur, J. N., de Bruyn, A. G. & Narasimha, D., 1999, A&A, 343, L79
Chengalur, J. N. & Kanekar, N., 2003, A&A, 403, L43
Cherchneff, I. & Dwek, E., 2009, ApJ, 703, 642
Churchwell, E. & Hollis, J. M., 1983, ApJ, 272, 591
Combes, F. & Wiklind, T., 1997, astro-ph/9711184
Combes, F., 2008, Ap&SS, 313, 321
Cox, P., Guesten, R. & Henkel, C., 1988, A&A, 206, 108
Cui, J., Bechtold, J., Ge, J. & Meyer, D. M., 2005, ApJ, 633, 649
Curran, S. J., Johansson, L. E. B., Bergman, P., Heikkilä, A. & Aalto, S., 2001, A&A, 367, 457
Curran, S. J., Murphy, M. T., Pihlström, Y. M., et al., 2004, MNRAS, 352, 563
Curran, S. J., Whiting, M. T., Murphy, M. T., et al., 2006, MNRAS, 371, 431
Curran, S. J., Whiting, M. T., Combes, F., et al., 2011, MNRAS, in press, [arXiv:1106.0578]
de Jong, T., Boland, W. & Dalgarno, A., 1980, A&A, 91, 68
Dickens, J. E, Irvine, W. M., De Vries, C. H. & Ohishi, M., 1997, ApJ, 479, 307
Drinkwater, M. J., Combes, F. & Wiklind, T., 1996, A&A, 312, 771
Falco, E. E., Impey, C. D., Kochanek, C. S., et al., 1999, ApJ, 523, 617
Flambaum, V. V. & Kozlov, M. G., 2007, Phys. Rev. Lett., 99, 801
Fossé, D., Cernicharo, J., Gérin, Maryvonne & Cox, P., 2001, ApJ, 552, 168
Fruchter, A. S. & Hook, R. N., 2002, PASP, 114, 144
Fuente, A., Cernicharo, J., Barcia, A. & Gomez-Gonzalez, J., 1990, A&A, 231, 151
García-Burillo, S., Martín-Pintado, J., Fuente, A., Usero, A. & Neri, R., 2002, apj, 575, L55
Ge, J. Bechtold, J., & Black, J. H., 1997, ApJ, 474, 67
Gérin, M., Phillips, T. G., Benford, D. J., et al., 1997, ApJ, 488, L31
Gérin, M., Goicoechea, J. R., Pety, J. & Hily-Blant, P., 2009, A&A, 494, 977
Gérin, M., Kaźmierczak, M., Jastrzebska, M., et al., 2011, A&A, 525, 116
Godfrey, P. D., Brown, R. D., Robinson, B. J. & Sinclair, M. W., 1973, Astrophys. Lett., 13, 119
Gottlieb, C. A. & Ball, J. A., 1973, ApJ, 184, 59
Gottlieb, C. A., Ball, J. A., Gottlieb, E. W., Lada, C. J. & Penfield, H., 1975, ApJ, 200, 147
Guélin, M., Green, S. & Thaddeus, P., 1978, ApJ, 224, L27
Guélin, M., Salomé, P., Neri, R., et al., 2007, A&A, 462, L45
Hatchell, J. & Viti, S., 2002, A&A, 381, L33
Heikkilä, A., Johansson, L. E. B. & Olofsson, H., 1999, A&A, 344, 817
Henkel, C., Jacq, T., Mauersberger, R., Menten, K. M. & Steppe, H., 1987, A&A, 188, L1
Henkel, C., Mauersberger, R., Wiklind, T., et al., 1993, A&A, 268, L17
Henkel, C., Braatz, J. A., Menten, K. M. & Ott, J., 2008, A&A, 485, 451
Henkel, C., Menten, K. M., Murphy, M. T., et al., 2009, A&A, 500, 725
Ilyushin, V. & Lovas, F. J., 2007, Journal of Physical and Chemical Reference Data, 36, 1141

Irvine, W. M., Hoglund, B., Friberg, P., Askne, J. & Ellder, J., 1981, ApJ, 248, L113
Irvine, W. M., Friberg, P., Hjalmarson, A., et al., 1988, ApJ, 334, 107
Irvine, W. M., Friberg, P., Kaifu, N., et al., 1989, ApJ, 342, 871
Jansen, P., Xu, L.-H., Kleiner, I., Ubachs, W. & Bethlem, H. L., 2011, Phys. Rev. Lett., 106, 0801
Jauncey, D. L., Reynolds, J. E., Tzioumis, A. K., et al., 1991, Nature, 352, 132
Jin, C., Garrett, M. A., Nair, S., et al., 2003, MNRAS, 340, 1309
Kaifu, N., Morimoto, M., Nagane, K., et al., 1974, ApJ, 191, L135
Kaifu, N., Ohishi, M., Kawaguchi, K., et al., 2004, PASJ, 56, 69
Kalenskii, S. V., Promislov, V. G., Alakoz, A. V., Winnberg, A. & Johansson, L. E. B., 2000, Astronomy Reports, vol. 44, 725
Kanekar, N., Carilli, C. L., Langston, G. I., et al., 2005, Phys. Rev. Lett., 95, 1301
Kanekar, N., 2011, ApJ, 728, L12
Kobayashi, C., Karakas, A. I. & Umeda, H., 2011, MNRAS, in press
Koopmans, L. V. E. & de Bruyn, A. G., 2005, MNRAS, 360, L6
Langer, W. D., Graedel, T. E., Frerking, M. A. & Armentrout, P. B., 1984, ApJ, 277, 581
Lidman, C., Courbin, F., Meylan, G., et al., 1999, ApJ, 514, 57
Lindberg, J. E., Aalto, S., Costagliola, F., et al., 2011, A&A, 527, 150
Lis, D. C., Wootten, A., Gérin, M. & Roueff, E., 2010, ApJ, 710, L49
Liszt, H. S., Pety, J. & Lucas, R., 2008, A&A, 486, 493
Liszt, H. S., Lucas, R. & Black, J. H., 2004, A&A, 428, 117
Liszt, H. S. & Lucas, R., 2001, A&A, 370, 576
Lodders, K., 2003, ApJ, 591, 1220
Lovell, J. E. J., Reynolds, J. E., Jauncey, D. L., et al., 1996, ApJ, 472, 5
Lovell, J. E. J., Jauncey, D. L., Reynolds, J. E., et al., 1998, ApJ, 508, L51
Lu, L., Sargent, W. L. W., Womble, D. S. & Barlow, T. A., 1996, ApJ, 457, L1
Lucas, R. & Liszt, H., 1998, A&A, 337, 246
Lucas, R. & Liszt, H. S., 2000a, A&A, 355, 327
Lucas, R. & Liszt, H. S., 2000b, A&A, 358, 1069
Lucas, R. & Liszt, H. S., 2002, A&A, 384, 1054
McGonagle, D., Irvine, W. M. & Ohishi, M., 1994, ApJ, 422, 621
McGonagle, D. & Irvine, W. M., 1997, ApJ, 477, 711
Madden, S. C., Irvine, W. M., Swade, D. A., et al., 1989, AJ, 97, 1403
Maier, J. P., Walker, G. A. H., Bohlender, D. A., et al., 2011, ApJ, 726, 41
Martín, S., Mauersberger, R., Martín-Pintado, J., García-Burillo, S. & Henkel, C., 2003, A&A, 411, L465
Martín, S., Mauersberger, R., Martín-Pintado, J., Henkel, C. & García-Burillo, S., 2006, ApJS, 164, 450
Martín, S., Martín-Pintado, J. & Viti, S., 2009, ApJ, 706, 1323
Martín, S., Aladro, R., Martín-Pintado, J. & Mauersberger, R., 2010, A&A, 522, 62
Mathur, S. & Nair, S., 1997, ApJ, 484, 140
Matthews, H. E. & Sears, T. J., 1983, ApJ, 267, L53
Matthews, H. E., Friber, P. & Irvine, W. M., 1985, ApJ, 290, 609
Matthews, H. E. & Irvine, W. M., 1985, ApJ, 298, L61
Mauersberger, R., Henkel, C., Walmsley, C. M., Sage, L. J. & Wiklind, T., 1991, A&A, 247, 307
Menten, K. M. & Reid, M. J., 1996, ApJ, 465, L99
Menten, K. M., Carilli, C. L., Reid, M. J., 1999, ASP Conf. Ser., 156, 218
Menten, K. M., Güsten, R., Leurini, S., et al., 2008, A&A, 492, 725
Minh, Y. C., Irvine, W. M. & Brewer, M. K., 1991, A&A, 244, 181
Molaro, P., Levshakov, S. A., Dessauges-Zavadsky, M. & D'Odorico, S., 2002, A&A, 381, L64
Müller, H. S. P., Thorwirth, S., Roth, D. A. & and Winnewisser, G., 2001, A&A, 370, L49
Muller, S., Guélin, M., Dumke, M., et al., 2006, A&A, 458, 417
Muller, S., Guélin, M., Combes, F. & Wiklind, T., 2007, A&A, 468, L53
Muller, S. & Guélin, M., 2008, A&A, 491, 739
Murphy, M. T., Curran, S. J. & Webb, J. K., 2003, MNRAS, 342, 830
Murphy, M. T., Flambaum, Victor V., Muller, S. & Henkel, C., 2008, Science, 320, 1611
Nair, S., Jin, C. & Garrett, M. A., 2005, MNRAS, 362, 1157
Noterdaeme, P., Petitjean, P., Srianand, R., et al., 2011, A&A, 526, L7
Nummelin, A., Bergman, P., Hjalmarson, Å., et al., 2000, ApJS, 128, 213
Ohishi, M., Irvine, W. M. & Kaifu, N., 1992, IAU Symp. 150, 171
Olmi, L., Cesaroni, R. & Walmsley, C. M., 1993, A&A, 276, 489
Patel, N. A., Young, K. H., Gottlieb, C. A., Thaddeus, P., Wilson, Robert W., et al., 2011, ApJS, 193, 17
Patnaik, A. R., Browne, I. W. A., King, L. J., et al., 1993, MNRAS, 261, 435
Pickett, H. M., Poynter, I. R. L., Cohen, E. A., et al., 1998, J. Quant. Spec. Radiat. Transf., 60, 883
Riechers, D. A., Walter, F., Carilli, C. L., et al., 2006, ApJ, 645, L13
Rodgers, S. D. & Charnley, S. B., 2008, ApJ, 689, 1448
Rodgers, S. D., Charnley, S. B., 2008, MNRAS, 385, L48
Roth, K. C. & Bauer, J. M., 1999, ApJ, 515, L57
Ruiterkamp, R., Charnley, S. B., Butner, H. M., et al., 2007, Ap&SS, 310, 181
Rydbeck, O. E. H., Hjalmarson, A., Rydbeck, G., et al., 1980, ApJ, 235, 171
Saito, S., Kawaguchi, K., Yamamoto, S., et al., 1987, ApJ, 317, L115
Sakai, N., Saruwatari, O., Sakai, T., Takano, S. & Yamamoto, S., 2010, A&A, 512, 31
Salter, C. J., Ghosh, T., Catinella, B., et a., 2008. AJ, 136, 389
Schilke, P., Pineau des Forêts, G., Walmsley, C. M. & Martín-Pintado, J., 2001, A&A, 372, 291
Sinclair, M. W., Fourikis, N., Ribes, J. C., et al., Aust. J. Phys., 26, 85
Snyder, L. E. & Buhl, D., 1972, ApJ, 177, 619
Snyder, L. E. & Buhl, D., 1973, Nature, 243, 45
Snyder, L. E., Hollis, J. M. & Ulich, B. L., 1976, ApJ, 208, L91
Solomon, P. M., Jefferts, K. B., Penzias, A. A. & Wilson, R. W., 1971, ApJ, 168, L107
Spergel, D. N., Verde, L., Peiris, H. V., et al., 2003, ApJS, 148, 175
Subrahmanyan, R., Narasimha, D., Pramesh-Rao, A. & Swarup, G., 1990, MNRAS, 246, 263
Takagi, K. & Kojima, T., 1973, ApJ, 181, 91
Thaddeus, P., Gottlieb, C. A., Hjalmarson, A., et al., 1985, ApJ, 294, L49
Thaddeus, P., Vrtilek, J. M. & Gottlieb, C. A., 1985, ApJ, 299, L63
Tucker, K. D., Kutner, M. L. & Thaddeus, P., 1974, ApJ, 193, L115
Turner, B. E., 1971, ApJ, 163, 35
Turner, B. E., 1977, ApJ, 213, 75
Turner, B. E., 1991, ApJS, 76, 617
Turner, B. E., 1994, ApJ, 430, 727
Turner, B. E., 1995a, ApJ, 449, 635
Turner, B. E., 1995b, ApJ, 455, 556
Turner, B. E., 1996, ApJ, 468, 694
Turner, B. E., 1998, ApJ, 501, 731
Turner, B. E., Lee, H.-H. & Herbst, E., 1998, ApJS, 115, 91
Turner, B. E., Terzieva, R. & Herbst, E., 1999, ApJ, 518, 699
Turner, B. E., 2000, ApJ, 542, 837
Turner, B. E., Herbst, E. & Terzieva, R., 2000, ApJS, 126, 427
Uzan, J.-P., 2011, Living Reviews in Relativity, 14, 2
van Dishoeck, E. F., Blake, G. A., Jansen, D. J. & Groesbeck, T. D., 1995, ApJ, 447, 760
Viti, S., Caselli, P., Hartquist, T. W. & Williams, D. A., 2001, A&A, 370, 1017
Wagg, J., Wilner, D. J., Neri, R., Downes, D. & Wiklind, T., 2005, ApJ, 643, L13
Walter, F., Bertoldi, F., Carilli, C., et al., 2003, Nature, 424, 406
Wang, M., Henkel, C., Chin, Y.-N., et al., 2004, A&A, 422, 883
Wang, M., Chin, Y.-N., Henkel, C., Whiteoak, J. B. & Cunningham, M., 2009, ApJ, 690, 580
Wiklind, T. & Combes F. 1995, A&A, 299, 382
Wiklind T. & Combes F. 1996a, A&A, 315, 86
Wiklind T. & Combes F. 1996b, Nature, 379, 139
Wiklind T. & Combes F. 1997, A&A, 328, 48
Wiklind T. & Combes F. 1998, ApJ, 500, 129
Wiklind, T. & Combes, F., 1999, [arXiv:astro-ph/9909314]
Winn, J. N., Kochanek, C. S., McLeod, B. A., et al., 2002, ApJ, 575, 103
Woods, R. C., Gudeman, C. S., Dickman, R. L., et al., 1983, ApJ, 270, 583
Yamamoto, S., Saito, S., Ohishi, M., et al., 1987, ApJ, 322, L55
York, T., Jackson, N., Browne, I. W. A., Wucknitz, O. & Skelton, J. E., 2005, MNRAS, 357, 124
Ziurys, L. M., Friberg, P. & Irvine, W. M., 1989, ApJ, 343, 201
Ziurys, L. M. & Apponi, A. J., 1995, ApJ, 455, L73

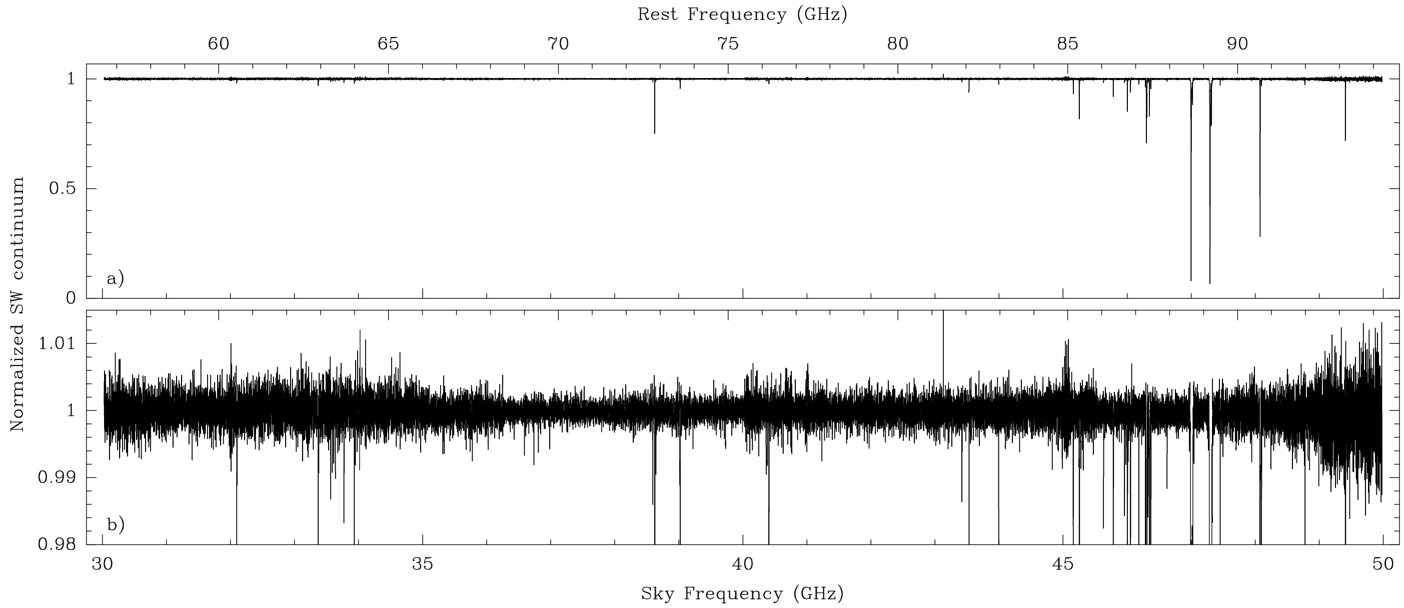

Fig. 2. a) Full 30–50 GHz spectral band observed toward PKS 1830−211 with the ATCA, normalized to the continuum flux of the SW image of the quasar (38% of the total flux). b) Same spectral interval, but limited to a scale of a few percent of the SW continuum intensity, to illustrate the noise level over the band. The rest-frame frequency axis is given on top of the figure.

Table 3. Census of species detected toward FG0.89SW.

1 atom	2 atoms	3 atoms	4 atoms	5 atoms	6 atoms	7 atoms
(H) (d)	(OH) (d)	(H_2O) (h)	(NH_3) (gh)	$\mathbf{CH_2NH}$	$\mathbf{CH_3OH}$	$\underline{\mathbf{CH_3NH_2}}$
(C) (i)	(CO) (bci)	C_2H (e)	H_2CO (ce)	c-C_3H_2 (e)	$\mathbf{CH_3CN}$	$\underline{\mathbf{CH_3C_2H}}$
	(CS) (af)	HCN (aef) △	$\underline{\mathbf{l\text{-}C_3H}}$	$\underline{\mathbf{l\text{-}C_3H_2}}$		$\underline{\mathbf{CH_3CHO}}$
	SiO (j) †	HNC (aef) ◇	**HNCO**	$\underline{\mathbf{H_2CCN}}$		
	NS	N_2H^+ (a)	$\mathbf{H_2CS}$	$\underline{\mathbf{H_2CCO}}$		
	SO	HCO^+ (aef) ○		$\underline{\mathbf{C_4H}}$		
	$\underline{\mathbf{SO^+}}$	**HCO**		HC_3N (ej)		
		$\mathbf{HOC^+}$				
		(H_2S) (f)				
		$\mathbf{C_2S}$				

Notes. In parenthesis, species detected in other studies; bold face, new detections; underlined, first extragalactic detections. ○ including $H^{13}CO^+$, $HC^{18}O^+$, and $HC^{17}O^+$; △ including $H^{13}CN$ and $HC^{15}N$; ◇ including $HN^{13}C$ and $H^{15}NC$; † including ^{29}SiO.

References. (a) Wiklind & Combes (1996b); (b) Gérin et al. (1997); (c) Wiklind & Combes (1998); (d) Chengalur et al. (1999); (e) Menten et al. (1999); (f) Muller et al. (2006), including isotopologues; (g) Henkel et al. (2008); (h) Menten et al. (2008); (i) Bottinelli et al. (2009); (j) Henkel et al. (2009).

Table 4. Molecular data for species detected toward the SW absorption.

Molecule	μ (Debye)	$Q_{5.14K}$ [a]	N_{line} [b]	V_0 (km s^{-1})	ΔV (km s^{-1})	T_{rot} [c] (K)	N_{COL} [c] (10^{12} cm^{-2})	N_{LTE} [d] (10^{12} cm^{-2})	Note
C_2H	0.77	2.81	6	−0.45 (0.03)	20.9 (0.1)	–	–	1248.5 (1.4)	hfs,CDMS
HCN	2.99	2.78	1	−2.83 (0.01)	28.9 (0.0)	–	–	304.1 (0.5)	CDMS
$H^{13}CN$	2.99	2.84	1	−2.27 (0.14)	21.4 (0.3)	–	–	8.4 (0.1)	CDMS
$HC^{15}N$	2.99	2.85	1	–	–	–	–	1.6 (0.1)	CDMS
HNC	3.05	2.73	1	−1.75 (0.02)	20.8 (0.1)	–	–	101.8 (0.3)	CDMS
$HN^{13}C$	3.05	2.82	1	–	–	–	–	2.2 (0.1)	CDMS
$H^{15}NC$	3.05	2.77	1	–	–	–	–	0.3 (0.1)	JPL
N_2H^+	3.40	2.66	1	−3.29 (0.12)	21.0 (0.3)	–	–	23.3 (0.3)	CDMS
HCO^+	3.90	2.77	1	−2.43 (0.02)	32.4 (0.0)	–	–	175.1 (0.3)	CDMS
$H^{13}CO^+$	3.90	2.83	1	−1.83 (0.07)	18.4 (0.2)	–	–	8.3 (0.1)	CDMS
$HC^{18}O^+$	3.90	2.88	1	–	–	–	–	3.6 (0.1)	CDMS
$HC^{17}O^+$	3.90	2.82	1	–	–	–	–	0.2 (0.0)	CDMS
HOC^+	2.77	2.76	1	−0.78 (0.39)	20.5 (0.9)	–	–	3.2 (0.1)	CDMS
HCO	1.36	2.83	4	1.44 (0.59)	18.1 (1.4)	–	–	13.0 (1.8)	hfs,JPL
CH_2NH	1.53	14.63	1	−0.71 (0.36)	13.8 (0.8)	–	–	14.9 (0.8)	JPL
H_2CO(p)	2.33	3.30	1	−1.00 (0.04)	20.3 (0.1)	–	–	59.8 (0.2)	CDMS
CH_3NH_2(o)	1.26	208.60	2	−6.19 (1.64)	20.6 (3.9)	$4.0^{+11.0}_{-3.0}$	$6.0^{+18.0}_{-4.0}$	15.0 (3.1)	JPL
CH_3NH_2(p)	1.26	69.84	1	–	–	–	–	17.1 (3.9)	JPL
CH_3OH	1.44	6.97	1	−5.26 (0.51)	21.2 (1.2)	–	–	170.0 (8.3)	CDMS
l-C_3H	3.55	43.53	4	0.18 (0.50)	17.5 (1.0)	–	–	7.1 (0.1)	hfs,CDMS
c-C_3H_2(o)	3.43	22.57	2	−0.94 (0.07)	18.7 (0.2)	$5.6^{+0.4}_{-0.4}$	$32.0^{+4.0}_{-4.0}$	39.1 (0.3)	JPL
c-C_3H_2(p)	3.43	7.53	2	–	–	$5.4^{+1.0}_{-1.0}$	$10.5^{+3.5}_{-3.0}$	13.8 (0.2)	JPL
l-C_3H_2(o)	4.10	4.30	3	−1.93 (0.00)	21.1 (2.6)	$5.3^{+11.5}_{-3.0}$	$1.0^{+1.5}_{-0.5}$	1.5 (0.2)	CDMS
l-C_3H_2(p)	4.10	10.64	1	–	–	–	–	0.6 (0.2)	CDMS
H_2CCN(o)	3.50	197.52	2	−1.83 (2.03)	17.9 (4.5)	$3.0^{+3.1}_{-1.2}$	$1.0^{+0.9}_{-0.3}$	2.2 (0.3)	hfs,CDMS
CH_3CCH	0.78	85.55	1	0.59 (1.54)	15.6 (4.0)	–	–	60.0 (0.0)	CDMS
CH_3CN	3.92	80.51	2	−2.70 (0.00)	21.6 (0.0)	–	–	13.0 (0.0)	CDMS
H_2CCO(o)	1.42	4.71	4	−1.62 (0.99)	21.2 (2.3)	$2.6^{+1.1}_{-0.8}$	$5.0^{+2.0}_{-1.5}$	13.2 (1.1)	CDMS
HNCO	1.58	10.09	2	−5.12 (0.88)	22.0 (2.1)	–	–	6.2 (0.6)	CDMS
SiO	3.10	5.28	1	−2.29 (0.18)	20.6 (0.4)	–	–	7.5 (0.1)	CDMS
^{29}SiO	3.10	5.34	1	–	–	–	–	0.7 (0.2)	CDMS
CH_3CHO	2.42	55.30	9	−0.80 (0.73)	19.3 (1.7)	$7.5^{+12.0}_{-3.5}$	$15.0^{+30.0}_{-9.0}$	12.4 (0.9)	JPL
NS	1.81	26.85	10	−2.61 (0.78)	20.9 (1.8)	–	–	11.5 (0.6)	hfs,JPL
H_2CS(o)	1.65	2.58	2	−1.60 (0.79)	14.1 (1.9)	–	–	5.7 (0.8)	CDMS
H_2CS(p)	1.65	6.58	1	–	–	–	–	1.9 (0.3)	CDMS
SO	1.54	7.64	2	−1.01 (0.30)	19.7 (0.7)	$5.4^{+1.4}_{-1.4}$	$21.0^{+10.0}_{-10.0}$	25.6 (0.8)	CDMS
SO^+	2.30	11.06	2	1.54 (2.00)	20.0 (0.0)	–	–	1.7 (0.3)	JPL
C_4H	0.87	91.36	8	−1.05 (0.59)	18.5 (1.4)	$8.0^{+6.5}_{-3.5}$	$110.0^{+90.0}_{-30.0}$	131.3 (7.8)	CDMS
HC_3N	3.73	23.88	4	−3.90 (0.46)	21.4 (0.9)	$6.3^{+1.3}_{-1.3}$	$8.3^{+0.6}_{-0.6}$	11.2 (0.4)	CDMS
C_2S	2.88	24.71	3	−1.35 (0.83)	18.2 (2.0)	$5.7^{+12.0}_{-3.0}$	$3.2^{+4.6}_{-1.3}$	4.8 (0.4)	CDMS

Notes. (a) For species with ortho/para symmetry, the two forms were considered as distinct species and the partition function Q was thus calculated accordingly, with the weight factors g=3 for ortho form, and g=1 for para form. Hyperfine structure was taken into account when necessary.

(b) Number of lines detected or resolved (in the case of hyperfine structure).

(c) Rotation temperature and column density obtained from Monte Carlo simulations of rotation diagrams. Uncertainties correspond to a 95% confidence interval.

(d) Column density, assuming a rotation temperature of 5.14 K and LTE.

(e) Possibly underestimated due to the large opacity of the line.

Table 5. Line parameters and fitting results for the NE absorption component.

Species	V_0 (km s^{-1})	ΔV (km s^{-1})	$\int \tau dV$ (10^{-3} km s^{-1})	N_{LTE} (10^{12} cm^{-2})	$N^{\rm SW}_{LTE}/N^{\rm NE}_{LTE}$
HCO$^+$	−148.1 (0.1)	21.5 (0.1)	2897.0 (15.0)	7.5 (0.0)	23.4 (0.1)
HCN	−147.5 (0.1)	22.2 (0.2)	1656.0 (14.0)	7.3 (0.1)	41.5 (0.4)
HNC	−147.0 (0.5)	15.0 (1.0)	284.0 (14.0)	1.2 (0.1)	87.2 (4.3)
C$_2$H	−148.1 (0.5)	15.0 (0.0)	429.0 (9.0)	29.2 (0.6)	42.7 (0.9)
c-C$_3$H$_2$(o)	−147.5 (1.4)	16.0 (3.4)	84.0 (18.0)	0.8 (0.2)	47.9 (10.3)
c-C$_3$H$_2$(p)	−147.5 (1.4)	16.0 (3.4)	38.0 (11.0)	0.4 (0.1)	31.9 (9.2)
H$_2$CO(p)	−146.7 (0.7)	15.4 (1.7)	107.0 (10.0)	1.1 (0.1)	56.6 (5.3)
N$_2$H$^+$	−147.0 (0.0)	20.0 (0.0)	105.0 (0.0)	−0.3 (0.0)	−69.9 (0.0)
H^{13}CO$^+$	−147.0 (0.0)	20.0 (0.0)	39.0 (0.0)	−0.1 (0.0)	−78.9 (0.0)
H^{13}CN	−147.0 (0.0)	20.0 (0.0)	38.1 (0.0)	−0.2 (0.0)	−47.8 (0.0)

Notes. Negative values (except for velocities) represent either the (3 σ) upper (for N_{LTE}) or lower (for [SW]/[NE]) limits.

Table 6. Upper limits (3σ) for non-detections of some other interstellar species toward FG0.89SW.

Species	Rest Freq. (MHz)	μ (D)	$Q_{5.14K}$	S_{ul}	E_l/k_B (K)	$\int \tau dV$ (10^{-3} km s^{-1})	N_{LTE} (10^{12} cm^{-2})	[X]/[H$_2$] 10^{-11}
DCO$^+$	72039.314	3.90	3.3	1.00	0.0	$<$ 103.5	$<$ 0.1	$<$ 0.62
DCN	72414.696	2.99	3.3	1.00	0.0	$<$ 126.0	$<$ 0.3	$<$ 1.27
O$_2$	58446.587	–	5.0	0.00	23.6	$<$ 205.2	$<$ 265940.	$<$ 1329702.
C$_3$S	57806.705	3.70	37.4	10.02	12.5	$<$ 225.0	$<$ 4.5	$<$ 22.35
HC$_5$N	58577.354	4.33	80.8	22.00	29.5	$<$ 146.7	$<$ 56.6	$<$ 283.08
SO$_2$	69575.928	1.63	13.6	1.00	0.0	$<$ 109.8	$<$ 3.1	$<$ 15.70
OCS	72976.776	0.72	17.9	6.00	8.8	$<$ 140.4	$<$ 24.3	$<$ 121.31
^{34}SO	62074.047	1.54	7.7	1.93	1.4	$<$ 142.2	$<$ 1.9	$<$ 9.59
CH$_2$D$^+$	67273.575	0.33	0.4	4.50	18.6	$<$ 139.5	$<$ 23.0	$<$ 115.03
H$_2^{13}$CO(p)	71024.788	2.33	3.4	1.00	0.0	$<$ 100.8	$<$ 0.3	$<$ 1.73
HCNH$^+$	74111.305	0.29	3.2	1.00	0.0	$<$ 123.3	$<$ 25.5	$<$ 127.34
^{15}NNH$^+$	90263.840	3.40	2.7	1.00	0.0	$<$ 225.0	$<$ 0.2	$<$ 1.25
N^{15}NH$^+$	91205.696	3.40	2.7	1.00	0.0	$<$ 246.6	$<$ 0.3	$<$ 1.35
^{13}CCH	84119.331	0.77	23.1	2.00	0.0	$<$ 225.0	$<$ 21.5	$<$ 107.42
C^{13}CH	85229.332	0.77	23.0	2.00	0.0	$<$ 303.3	$<$ 28.6	$<$ 142.96
C$_2$H$_3$CN	56786.934	3.82	178.7	17.95	6.8	$<$1201.5	$<$ 20.0	$<$ 99.88
HC$_3$NH$^+$	60605.339	1.61	73.2	20.70	8.7	$<$ 148.5	$<$ 6.8	$<$ 34.03
C$_2$O	69069.473	1.31	28.5	3.84	3.3	$<$ 109.8	$<$ 5.1	$<$ 25.35

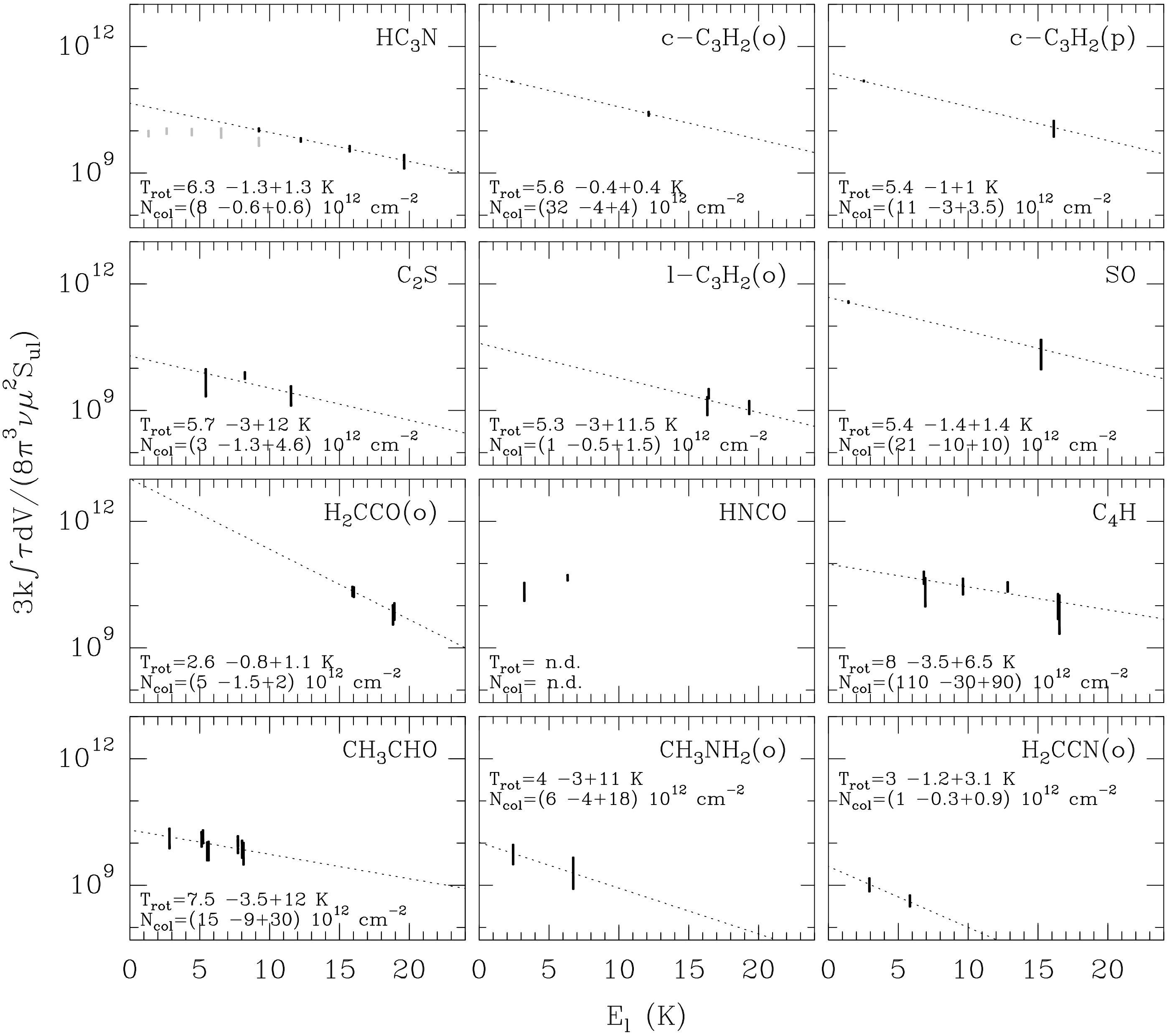

Fig. 4. Rotation diagrams. Uncertainties in the rotation temperatures and column densities were obtained from Monte Carlo simulations, and are given for a 95% confidence level. Data points for additional transitions of HC_3N observed by Henkel et al. (2009) are indicated in light grey (see B.24).

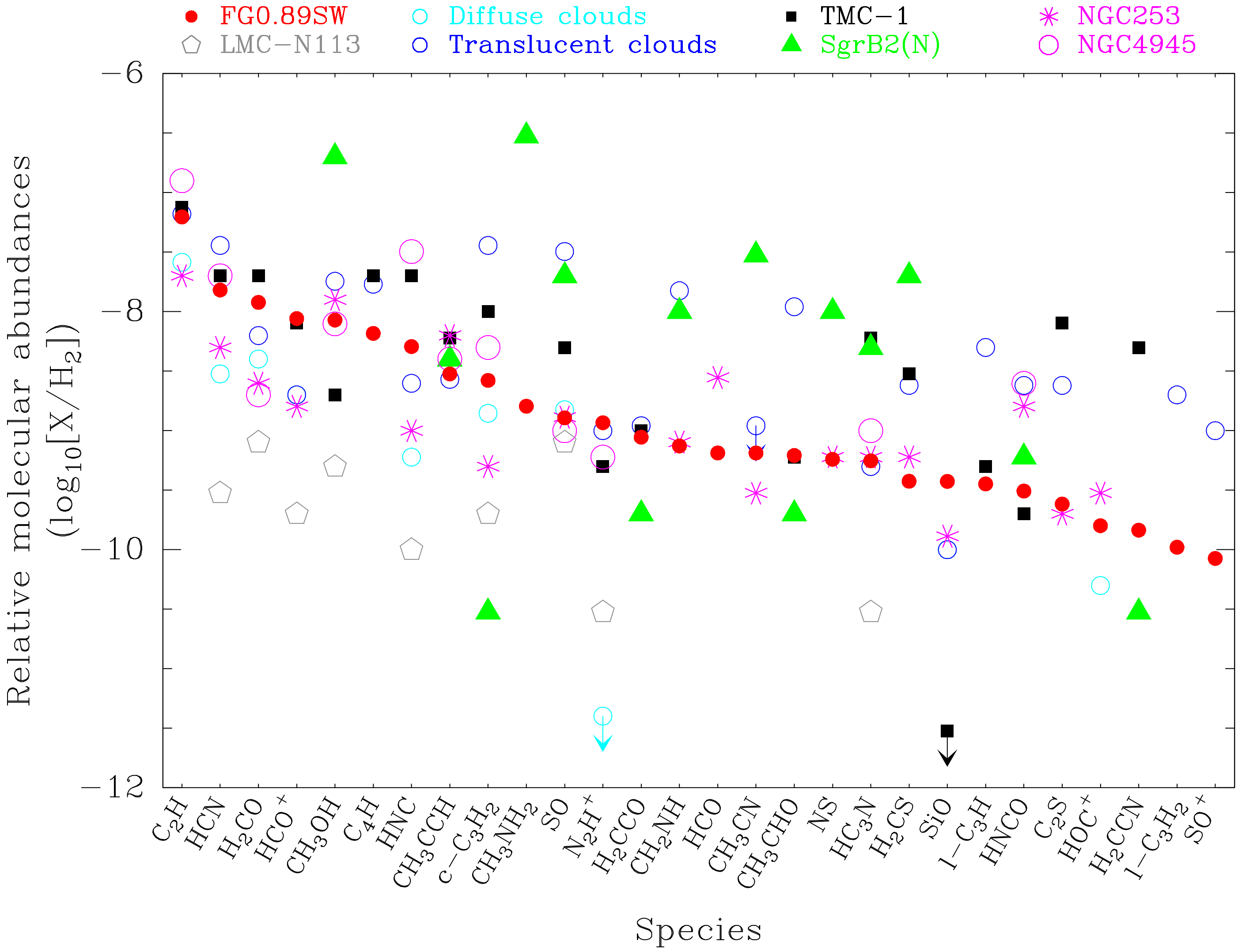

Fig. 8. Comparison of relative molecular abundances in FG0.89SW (from most to less abundant), diffuse clouds (Lucas & Liszt 2000a,b; Liszt & Lucas 2001; Lucas & Liszt 2002; Liszt et al. 2004), translucent clouds (Turner 2000), TMC-1 (Ohishi et al. 1992), Sgr B2(N) (Nummelin et al. 2000), LMC-N113 (Wang et al. 2009), and the nuclear region of the starburst galaxies NGC253 (Martín et al. 2006) and NGC4945 (Wang et al. 2004).

Table 9. Relative abundances [X]/[H_2] (10^{-11}).

Species	FG0.89SW	FG0.89NE	Diffuse clouds	Translucent clouds	TMC 1	Sgr B2(N)	LMC N113	NGC253	NGC4945
C_2H	6242.4	2924.5	2600.0	6600.0	7500.0	–	–	2000.0	12600.0
HCN	1520.4	733.0	300.0	3600.0	2000.0	–	30.0	500.0	2000.0
H_2CO	1196.3	422.4	400.0	630.0	2000.0	–	80.0	250.0	200.0
HCO^+	875.4	746.7	200.0	200.0	800.0	–	20.0	160.0	–
CH_3OH	849.9	–	–	1800.0	200.0	20000.0	50.0	1260.0	790.0
C_4H	656.7	–	–	1700.0	2000.0	–	–	–	–
HNC	509.2	116.8	60.0	250.0	2000.0	–	10.0	100.0	3200.0
CH_3CCH	300.0	–	–	270.0	600.0	400.0	–	630.0	400.0
c-C_3H_2	264.5	125.0	140.0	3600.0	1000.0	3.0	20.0	50.0	500.0
CH_3NH_2	160.6	–	–	–	–	30000.0	–	–	–
SO	128.1	–	150.0	3200.0	500.0	2000.0	80.0	130.0	100.0
N_2H^+	116.6	-33.4	-0.4	100.0	50.0	–	3.0	–	60.0
H_2CCO	88.3	–	–	110.0	100.0	20.0	–	–	–
CH_2NH	74.5	–	–	1500.0	–	1000.0	–	80.0	–
HCO	65.0	–	–	–	–	–	–	280.0	–
CH_3CN	65.0	–	–	-110.0	–	3000.0	–	30.0	–
CH_3CHO	62.0	–	–	1100.0	60.0	20.0	–	–	–
NS	57.5	–	–	–	–	1000.0	–	60.0	–
HC_3N	55.9	–	–	50.0	600.0	500.0	3.0	60.0	100.0
H_2CS	37.6	–	–	240.0	300.0	2000.0	–	60.0	–
SiO	37.5	–	10.0	10.0	-0.3	–	–	13.0	–
l-C_3H	35.7	–	–	500.0	50.0	–	–	–	–
HNCO	31.1	–	–	240.0	20.0	60.0	–	160.0	250.0
C_2S	24.2	–	–	240.0	800.0	–	–	20.0	–
HOC^+	15.9	–	5.0	–	–	–	–	30.0	–
H_2CCN	14.6	–	–	–	500.0	3.0	–	–	–
l-C_3H_2	10.5	–	–	200.0	–	–	–	–	–
SO^+	8.4	–	–	100.0	–	–	–	–	–

Notes. Negative values represent an upper limit. H_2 column densities of 2×10^{22} and 1×10^{21} cm^{-2} were assumed for FG0.89SW and FG0.89NE, respectively.

References. Diffuse clouds: Lucas & Liszt (2000a,b); Liszt & Lucas (2001); Lucas & Liszt (2002); Liszt et al. (2004); Translucent clouds: Turner (2000); TMC-1: Ohishi et al. (1992); SgrB2(N): Nummelin et al. (2000); LMC-N113: Wang et al. (2009), using $N(H_2)=2\times10^{22}$ cm^{-2}; NGC253: Martín et al. (2006); NGC4945: Wang et al. (2004).

Table 10. Abundance estimator.

Source	All species	Carbon chains	S-bearing species	Saturated species
FG0.89SW	0	0	0	0
LMC N113	-1.3(0.4) [9]	-1.2(0.1) [2]	– [1]	– [1]
Diffuse clouds	-0.5(0.3) [9]	– [1]	– [1]	– [0]
FG0.89NE	-0.4(0.2) [6]	– [1]	– [0]	– [0]
NGC253	-0.1(0.4) [19]	-0.3(0.4) [2]	0.0(0.1) [4]	– [1]
NGC4945	0.1(0.4) [11]	0.3(0.0) [2]	– [1]	– [1]
Transl. clouds	0.5(0.7) [22]	0.8(0.5) [5]	1.1(0.2) [4]	– [1]
TMC1	0.4(0.6) [19]	0.6(0.3) [4]	1.0(0.4) [3]	– [1]
Sgr B2N	0.5(1.1) [13]	-0.5(1.4) [2]	1.4(0.2) [3]	1.8(0.4) [2]

Notes. The abundance estimators were calculated according to Eq.5. The dispersion is given in parenthesis and the number of molecules detected in common between FG0.89SW and other sources for each sample is given within brackets.

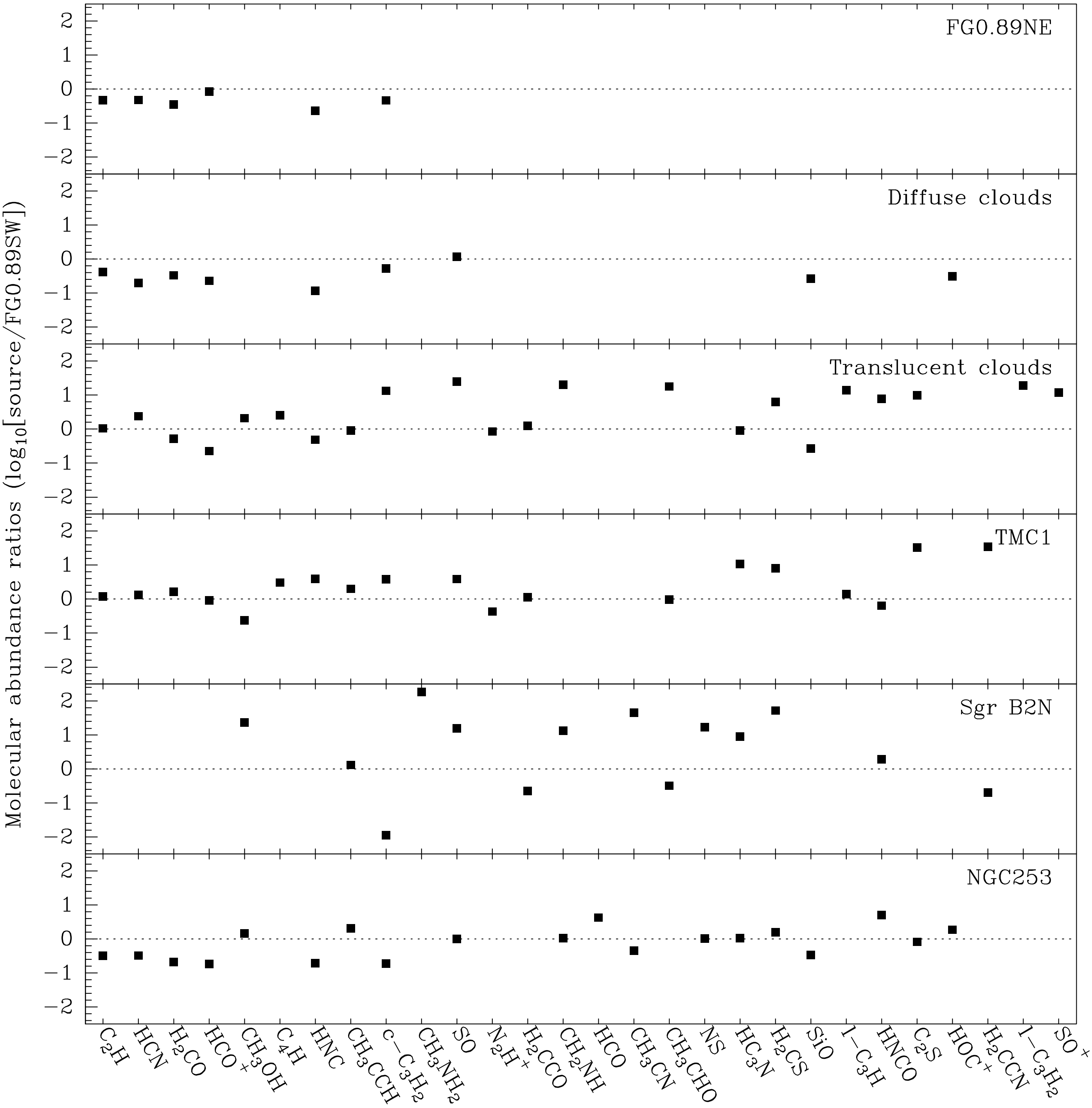

Fig. 9. Ratios of molecular abundances of FG0.89SW to other sources, detailed by species.

Appendix A: Spectral survey and line catalog

The full spectrum, from 30 to 50 GHz, is available on-line as an ASCII file at the *Strasbourg Astronomical Data Center* (CDS).

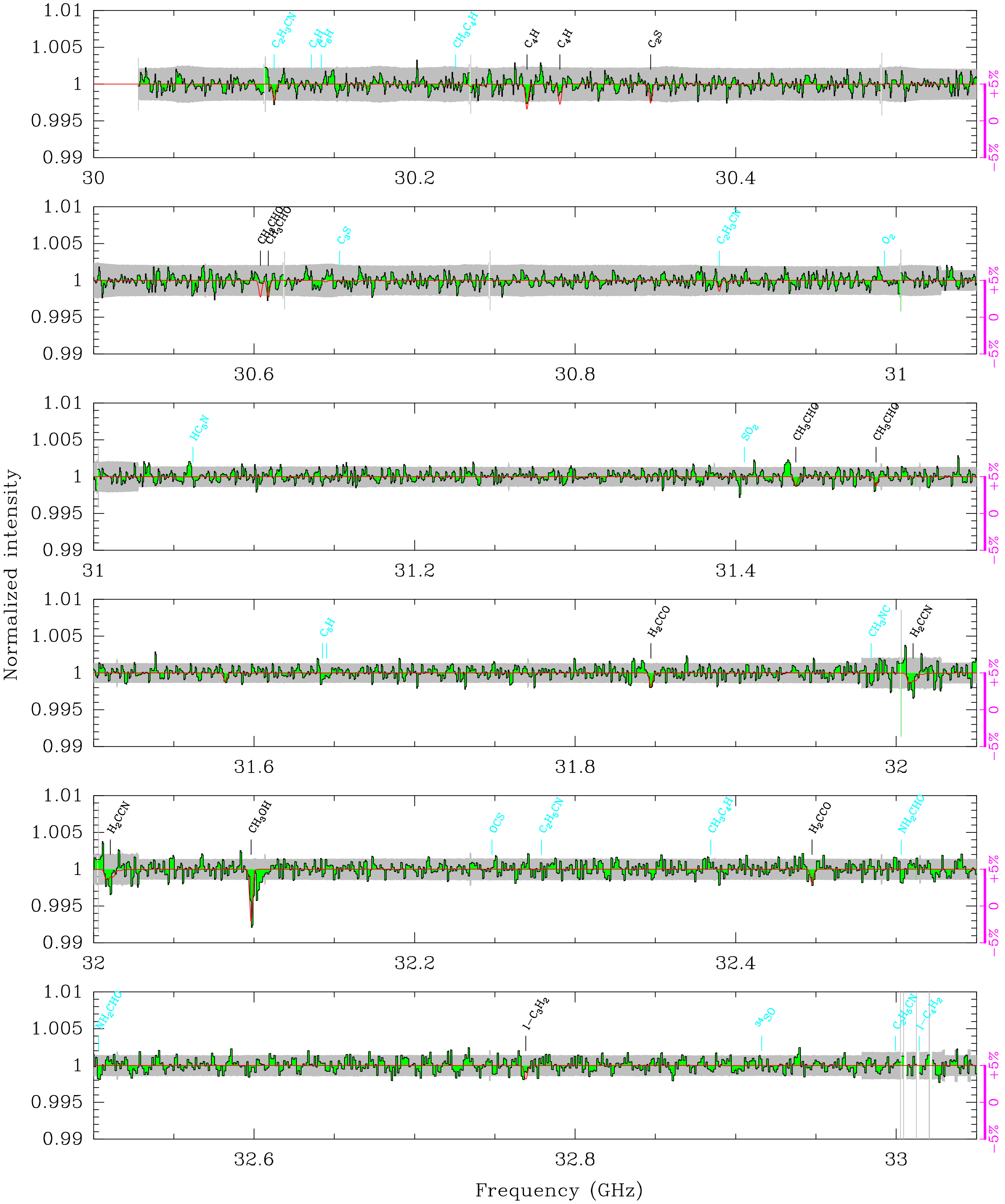

Fig. A.1. Spectrum of the ATCA 7 mm survey toward PKS 1830−211. The grey envelope indicates the 3 σ noise level. The LTE synthetic model, assuming T_{rot}=5.14 K for all molecules, is overlaid in red. The spectrum in magenta, offset at a level of 0.995, gives the relative differences between observations taken in September 2009 and March 2010, normalized to the average spectrum. The corresponding scale is given on the right of each box (±5%). Some non-detections are indicated in light blue.

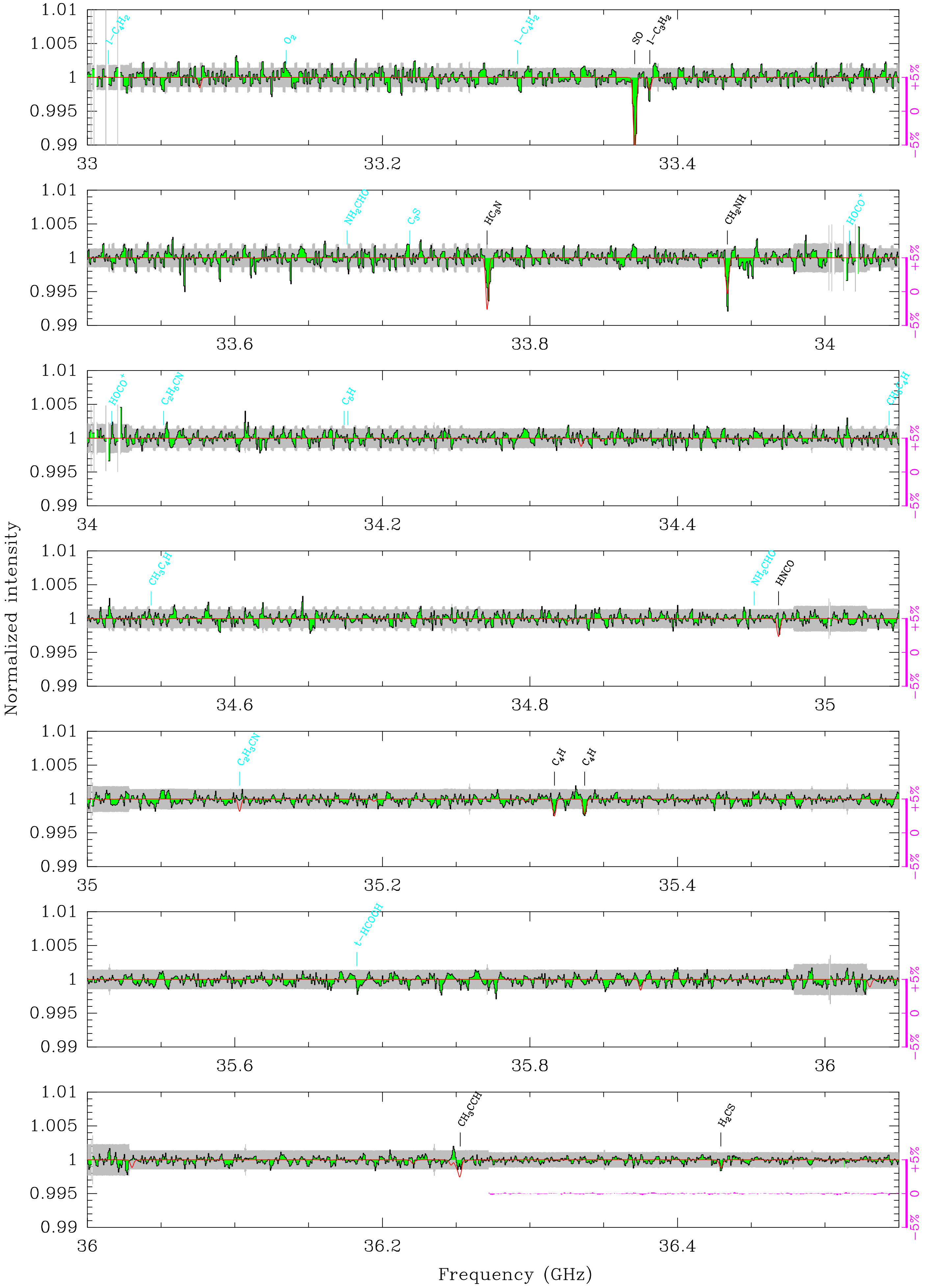

Fig. A.1. *Continued.*

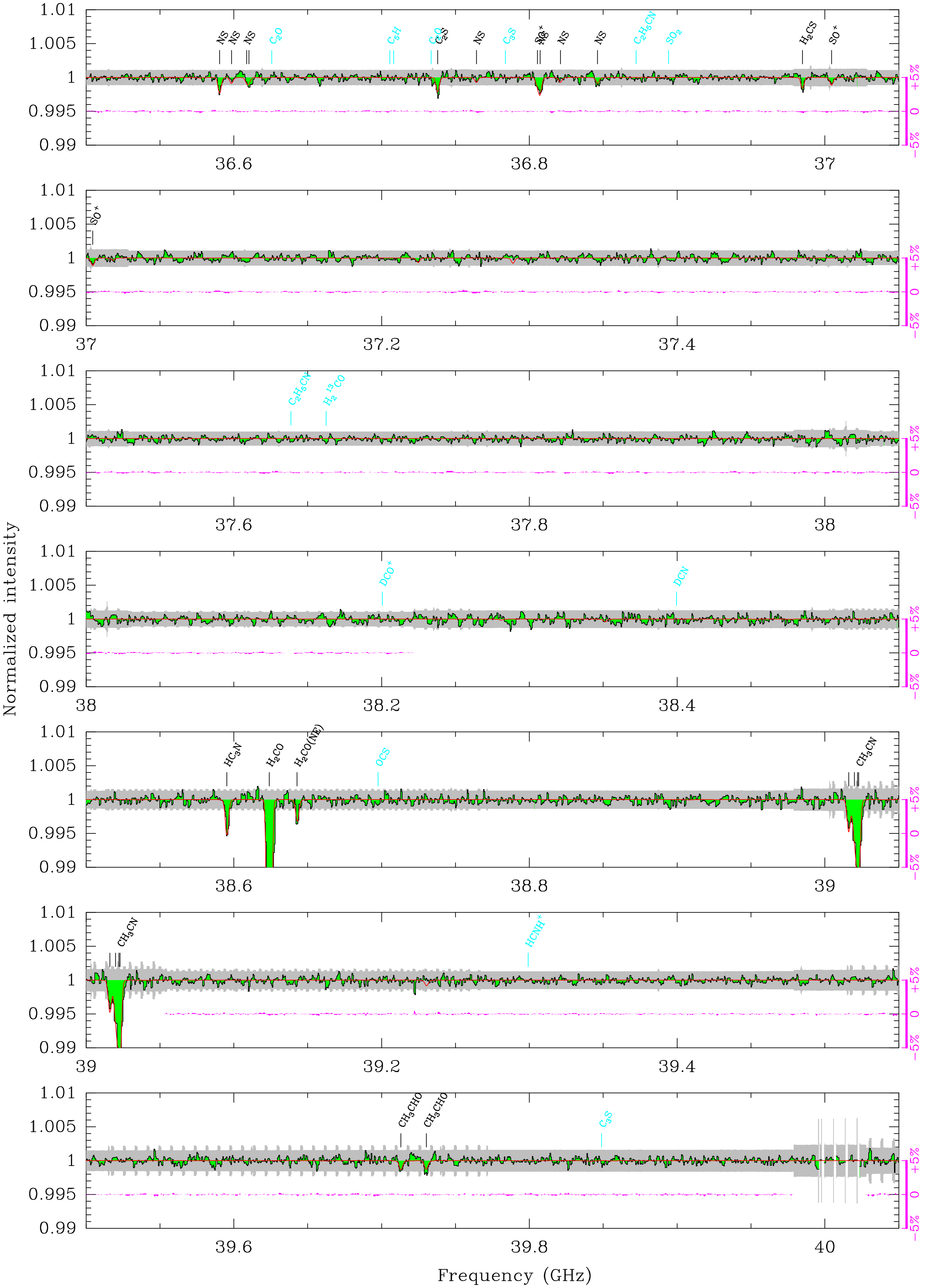

Fig. A.1. *Continued.*

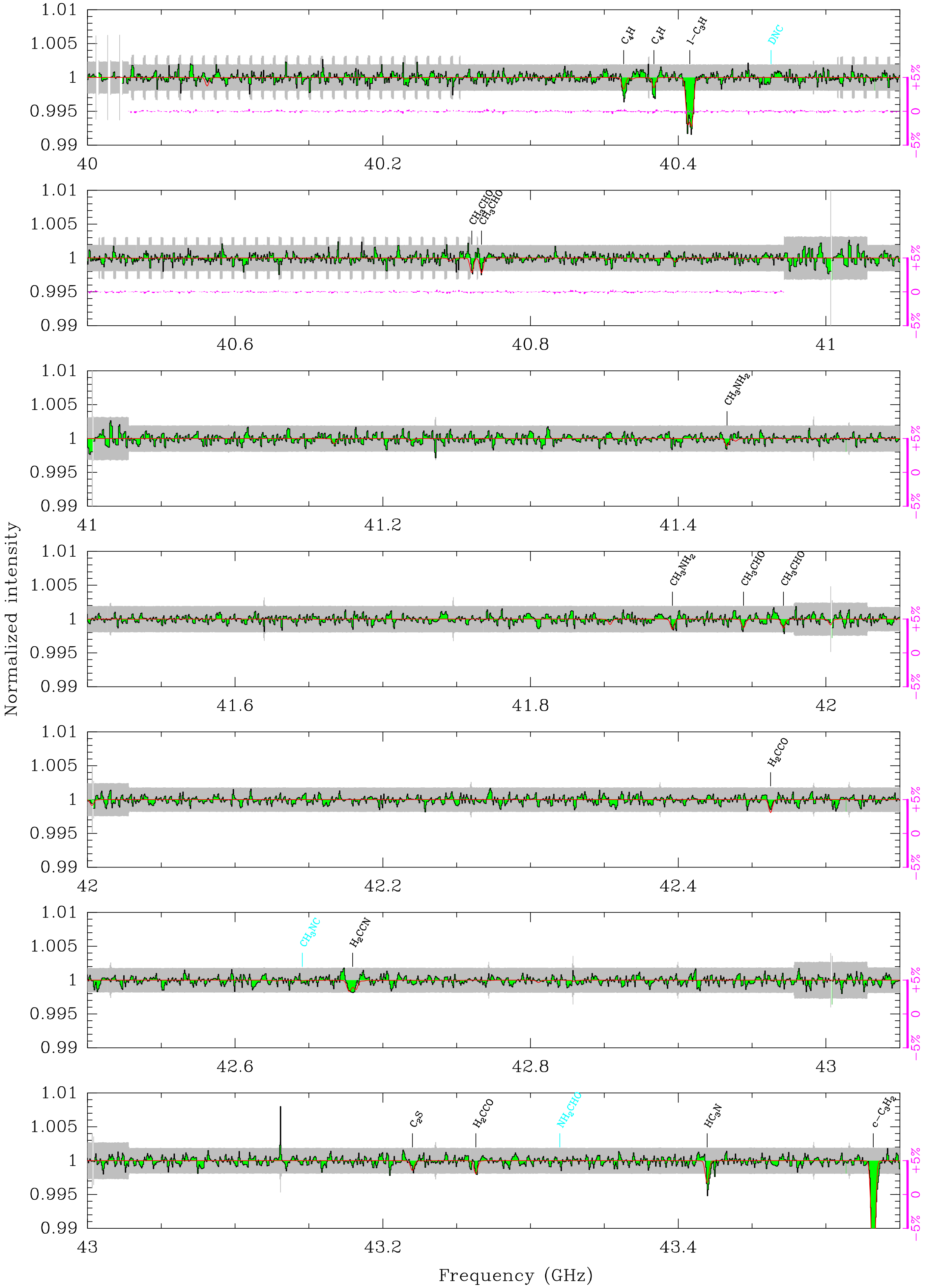

Fig. A.1. *Continued.*

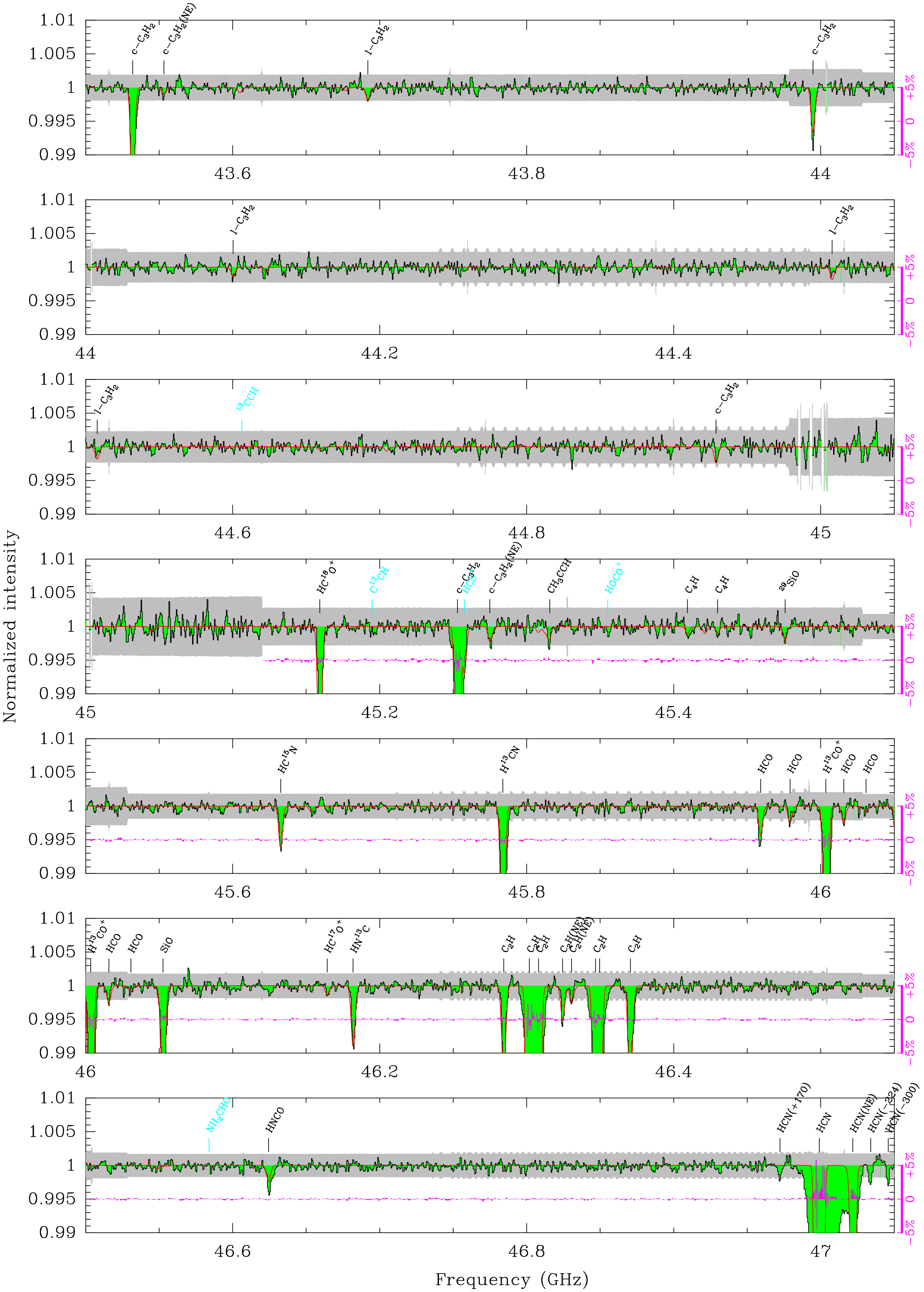

Fig. A.1. *Continued.*

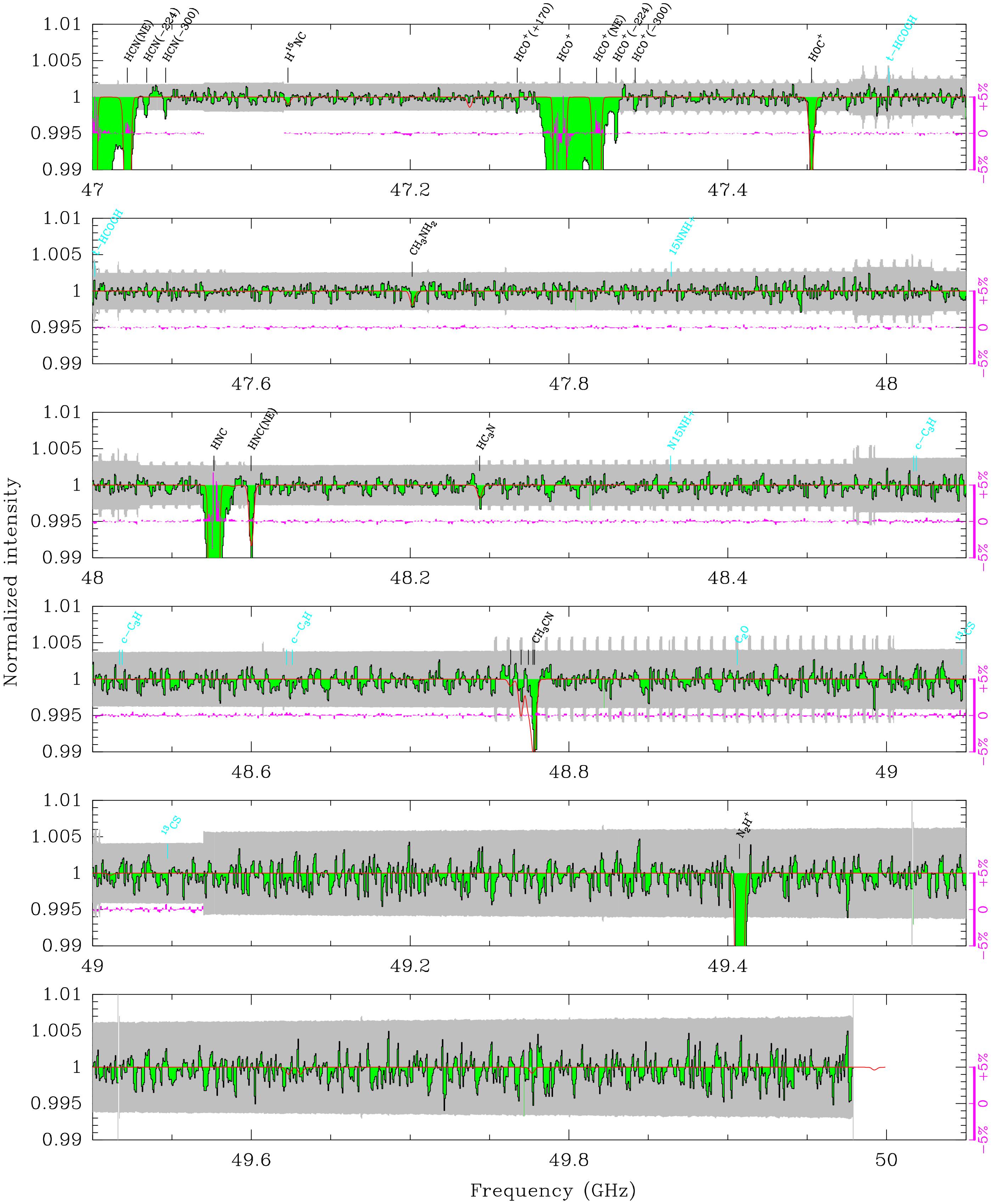

Fig. A.1. *Continued.*

Table A.1. Parameters and fitting results for lines detected toward FG0.89SW.

Rest Freq. (MHz)	Transition	S_{ul}	E_l/k_B (K)	V_0 (km s^{-1})	ΔV (km s^{-1})	$\int \tau \mathrm{d}V$ (10^{-3} km s^{-1})
87284.105	C_2H N=1-0 J=3/2-1/2 F=1-1	0.04	0.0	-0.45(0.03)	20.90(0.10)	777.(0.)
87316.898	C_2H N=1-0 J=3/2-1/2 F=2-1	0.42	0.0	–	–	7625.(21.)
87328.585	C_2H N=1-0 J=3/2-1/2 F=1-0	0.21	0.0	–	–	3799.(0.)
87401.989	C_2H N=1-0 J=1/2-1/2 F=1-1	0.21	0.0	–	–	3805.(0.)
87407.165	C_2H N=1-0 J=1/2-1/2 F=0-1	0.08	0.0	–	–	1528.(0.)
87446.470	C_2H N=1-0 J=1/2-1/2 F=1-0	0.04	0.0	–	–	780.(0.)
88631.602	HCN J=1-0	1.00	0.0	-2.83(0.01)	28.90(0.01)	68695.(113.)
86339.922	$H^{13}CN$ J=1-0	1.00	0.0	-2.27(0.14)	21.40(0.30)	1821.(25.)
86054.966	$HC^{15}N$ J=1-0	1.00	0.0	–	–	342.(19.)
90663.568	HNC J=1-0	1.00	0.0	-1.75(0.02)	20.80(0.10)	24767.(68.)
87090.825	$HN^{13}C$ J=1-0	1.00	0.0	–	–	498.(18.)
88865.715	$H^{15}NC$ J=1-0	1.00	0.0	–	–	70.(18.)
93173.392	N_2H^+ J=1-0	1.00	0.0	-3.29(0.12)	21.00(0.30)	7341.(84.)
89188.525	HCO^+ J=1-0	1.00	0.0	-2.43(0.02)	32.40(0.01)	67923.(102.)
86754.288	$H^{13}CO^+$ J=1-0	1.00	0.0	-1.83(0.07)	18.40(0.20)	3079.(25.)
85162.223	$HC^{18}O^+$ J=1-0	1.00	0.0	–	–	1310.(28.)
87057.535	$HC^{17}O^+$ J=1-0	1.00	0.0	–	–	69.(17.)
89487.414	HOC^+ J=1-0	1.00	0.0	-0.78(0.39)	20.50(0.90)	626.(24.)
86670.760	HCO $N_K=1_{01}$-0_{00} J=3/2-1/2 F=2-1	0.42	0.0	1.44(0.59)	18.10(1.40)	309.(22.)
86708.360	HCO $N_K=1_{01}$-0_{00} J=3/2-1/2 F=1-0	0.25	0.0	–	–	115.(19.)
86777.460	HCO $N_K=1_{01}$-0_{00} J=1/2-1/2 F=1-1	0.25	0.0	–	–	118.(20.)
86805.780	HCO $N_K=1_{01}$-0_{00} J=1/2-1/2 F=0-1	0.08	0.0	–	–	47.(19.)
63992.975	CH_2NH 1_{01}-0_{00}	2.25	0.0	-0.71(0.36)	13.80(0.80)	301.(16.)
72837.948	H_2CO(p) $J_{Ka,Kc}=1_{01}$-0_{00}	1.00	0.0	-1.00(0.04)	20.30(0.10)	6061.(22.)
78135.183	CH_3NH_2(o) 2_{13}-2_{02}	30.00	6.7	-6.19(1.64)	20.60(3.90)	60.(21.)
79008.422	CH_3NH_2(o) 1_{12}-1_{03}	18.00	2.4	–	–	84.(21.)
89956.068	CH_3NH_2(p) 1_{10}-1_{01}	6.00	2.1	–	–	110.(25.)
60531.489	CH_3OH 1_{01}-2_{-12} E	1.80	12.5	-5.26(0.51)	21.20(1.20)	431.(21.)
76198.726	l-C_3H J=7/2-5/2	3.85	4.2	0.18(0.50)	17.50(1.00)	222.(8.)
76199.928	l-C_3H J=7/2-5/2	2.85	4.2	–	–	167.(0.)
76204.182	l-C_3H J=7/2-5/2	3.85	4.2	–	–	222.(0.)
76205.103	l-C_3H J=7/2-5/2	2.85	4.2	–	–	167.(0.)
82966.200	c-C_3H_2(o) 3_{12}-3_{03}	2.93	12.1	-0.94(0.07)	18.70(0.20)	439.(27.)
85338.893	c-C_3H_2(o) 2_{12}-1_{01}	4.50	2.3	–	–	4013.(34.)
59557.896	c-C_3H_2(p) 3_{31}-3_{22}	1.37	16.1	–	–	71.(15.)
82093.559	c-C_3H_2(p) 2_{02}-1_{11}	1.37	2.5	–	–	1211.(20.)
61797.009	l-C_3H_2(o) 3_{13}-2_{12}	8.00	16.3	-1.93(0.00)	21.10(2.60)	72.(17.)
62950.993	l-C_3H_2(o) 3_{12}-2_{11}	8.00	16.4	–	–	132.(18.)
82395.089	l-C_3H_2(o) 4_{14}-3_{13}	11.25	19.3	–	–	117.(21.)
83165.345	l-C_3H_2(p) 3_{03}-2_{02}	4.00	6.0	–	–	83.(23.)
60366.000	H_2CCN(o) 3_{03}-2_{02}	54.00	2.9	-1.83(2.03)	17.90(4.50)	264.(47.)
80486.000	H_2CCN(o) 4_{04}-3_{03}	72.00	5.8	–	–	191.(30.)
85457.300	CH_3CCH $J_K=4_0$-3_0	10.00	8.2	0.59(1.54)	15.60(4.00)	130.(44.)
73577.451	CH_3CN $J_K=4_3$-3_3	7.00	69.6	-2.70(0.00)	21.60(0.00)	–
73584.543	CH_3CN $J_K=4_2$-3_2	6.00	33.9	–	–	–
73588.799	CH_3CN $J_K=4_1$-3_1	7.50	12.4	–	–	–
73590.218	CH_3CN $J_K=4_0$-3_0	8.00	5.3	–	–	–
91958.726	CH_3CN $J_K=5_4$-4_4	3.60	123.1	–	–	–
91971.130	CH_3CN $J_K=5_3$-4_3	12.80	73.1	–	–	–
91979.994	CH_3CN $J_K=5_2$-4_2	8.40	37.4	–	–	–
91985.314	CH_3CN $J_K=5_1$-4_1	9.60	16.0	–	–	–
91987.088	CH_3CN $J_K=5_0$-4_0	10.00	8.8	–	–	–
60058.127	H_2CCO(o) 3_{13}-2_{12}	8.00	15.9	-1.62(0.99)	21.20(2.30)	132.(18.)
61190.279	H_2CCO(o) 3_{12}-2_{11}	8.00	16.0	–	–	130.(18.)
80076.652	H_2CCO(o) 4_{14}-3_{13}	11.25	18.8	–	–	76.(19.)
81586.230	H_2CCO(o) 4_{13}-3_{12}	11.25	18.9	–	–	90.(20.)
65944.301	HNCO 3_{03}-2_{02}	3.00	3.2	-5.12(0.88)	22.00(2.10)	72.(17.)
87925.237	HNCO 4_{04}-3_{03}	4.00	6.3	–	–	247.(21.)
86846.960	SiO J=1-0	2.00	2.1	-2.29(0.18)	20.60(0.40)	1262.(22.)

Table A.1. Continued.

Rest Freq. (MHz)	Transition	S_{ul}	E_l/k_B (K)	V$_0$ (km s^{-1})	ΔV (km s^{-1})	$\int \tau$dV (10^{-3} km s^{-1})
85759.199	^{29}SiO J=1-0	2.00	2.1	–	–	112.(28.)
57722.670	CH_3CHO 3_{03}-2_{02} A	3.25	2.8	-0.80(0.73)	19.30(1.70)	99.(25.)
59285.370	CH_3CHO 3_{12}-2_{11} E	2.85	5.2	–	–	90.(16.)
59379.499	CH_3CHO 3_{12}-2_{11} A	2.88	5.1	–	–	81.(16.)
74891.677	CH_3CHO 4_{14}-3_{13} A	4.00	7.7	–	–	94.(17.)
74924.134	CH_3CHO 4_{14}-3_{13} E	4.00	7.7	–	–	122.(17.)
76866.436	CH_3CHO 4_{04}-3_{03} E	4.32	5.6	–	–	87.(21.)
76878.953	CH_3CHO 4_{04}-3_{03} A	4.32	5.5	–	–	85.(20.)
79099.313	CH_3CHO 4_{13}-3_{12} E	4.00	8.1	–	–	74.(20.)
79150.166	CH_3CHO 4_{13}-3_{12} A	4.00	8.0	–	–	89.(20.)
69002.890	NS J=3/2-1/2 F=5/2-3/2e	2.00	1.1	-2.61(0.78)	20.90(1.80)	129.(12.)
69017.991	NS J=3/2-1/2 F=3/2-1/2e	0.74	1.1	–	–	48.(0.)
69037.497	NS J=3/2-1/2 F=3/2-3/2e	0.59	1.1	–	–	38.(0.)
69040.324	NS J=3/2-1/2 F=1/2-1/2e	0.59	1.1	–	–	38.(0.)
69059.844	NS J=3/2-1/2 F=1/2-3/2e	0.07	1.1	–	–	5.(0.)
69283.195	NS J=3/2-1/2 F=1/2-3/2f	0.07	1.1	–	–	5.(0.)
69330.592	NS J=3/2-1/2 F=3/2-3/2f	0.59	1.1	–	–	49.(0.)
69411.943	NS J=3/2-1/2 F=5/2-3/2f	2.00	1.1	–	–	135.(14.)
69437.850	NS J=3/2-1/2 F=1/2-1/2f	0.59	1.1	–	–	40.(0.)
69485.223	NS J=3/2-1/2 F=3/2-1/2f	0.74	1.1	–	–	50.(0.)
69746.747	H_2CS(o) 2_{11}-1_{10}	4.50	14.8	-1.60(0.79)	14.10(1.90)	90.(13.)
68699.385	H_2CS(p) 2_{02}-1_{01}	2.00	1.6	–	–	67.(11.)
62931.800	SO J$_K$=2_1-1_0	1.92	1.4	-1.01(0.30)	19.70(0.70)	644.(20.)
86093.950	SO J$_K$=2_2-1_1	1.50	15.2	–	–	53.(18.)
69408.371	SO^+ J=3/2-1/2 e	1.31	0.0	1.54(2.00)	20.00(0.00)	63.(10.)
69783.846	SO^+ J=3/2-1/2 f	1.31	0.0	–	–	63.(0.)
57083.814	C_4H N=6-5 J=13/2-11/2	13.00	6.8	-1.05(0.59)	18.50(1.40)	165.(28.)
57122.461	C_4H N=6-5 J=11/2-9/2	11.00	6.9	–	–	79.(26.)
66600.700	C_4H N=7-6 J=15/2-13/2	15.00	9.6	–	–	114.(16.)
66639.313	C_4H N=7-6 J=13/2-11/2	13.00	9.6	–	–	143.(16.)
76117.438	C_4H N=8-7 J=17/2-15/2	17.00	12.8	–	–	177.(20.)
76156.031	C_4H N=8-7 J=15/2-13/2	15.00	12.8	–	–	150.(20.)
85634.012	C_4H N=9-8 J=19/2-17/2	19.00	16.4	–	–	89.(27.)
85672.578	C_4H N=9-8 J=17/2-15/2	17.00	16.5	–	–	66.(26.)
63686.052	HC_3N J=7-6	7.00	9.2	-3.90(0.46)	21.40(0.90)	396.(20.)
72783.822	HC_3N J=8-7	8.00	12.2	–	–	300.(17.)
81881.468	HC_3N J=9-8	9.00	15.7	–	–	236.(20.)
90979.023	HC_3N J=10-9	10.00	19.6	–	–	151.(28.)
57229.067	C_2S J$_N$=5_4-4_3	5.00	5.4	-1.35(0.83)	18.20(2.00)	84.(27.)
69281.115	C_2S J$_N$=6_5-5_4	6.00	8.2	–	–	142.(14.)
81505.170	C_2S J$_N$=7_6-6_5	7.00	11.5	–	–	72.(18.)

Notes. For species with hyperfine structure, the relative intensities were fixed, and the given uncertainty corresponds to that in the total integrated intensity.

Appendix B: Notes on individual molecules

In this section, we give short reviews of the different species and discuss constraints or new results obtained from this survey.

B.1. C_2H

The highly reactive ethynyl radical was first discovered and identified toward the Orion nebula by Tucker et al. (1974) based on its hyperfine structure, while it had still not been observed in the laboratory. C_2H has turned out to be both an ubiquitous and abundant species in the interstellar medium, including in diffuse clouds (Lucas & Liszt 2000b) where its abundance is of the order of a few 10^{-8} with respect to H_2.

The ground state transition N=1-0 at ν_0=87 GHz is decomposed into six components by hyperfine splitting. Toward PKS 1830−211, the strongest hyperfine components were previously observed by Menten et al. (1999) with the VLA, although at low spectral resolution. We detect here all six N=1-0 hyperfine components arising from the SW absorption, as well as the two strongest hyperfine components (the J=3/2-1/2, F=2-1 and F=1-0) related to the NE absorption at −147 km s^{-1} (see Fig.B.1). The absorption depths reflect the LTE relative intensities of the hyperfine components, indicating that the lines are optically thin.

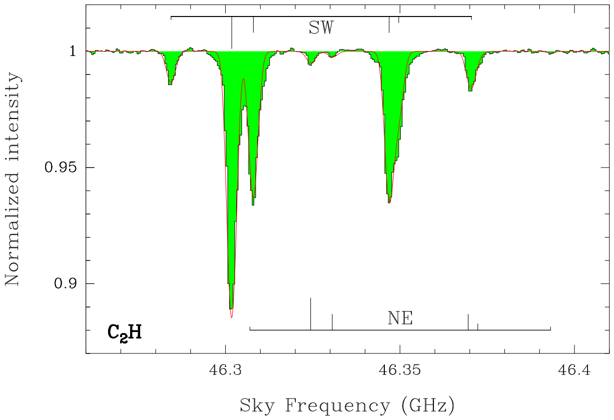

Fig. B.1. Spectrum of the C_2H N=1-0 line. The different hyperfine components are indicated with their relative intensities for the SW (*top*) and NE (*bottom*) absorptions. Note the clear detection of the two strongest hyperfine components arising from FG0.89NE. The red curve shows the LTE synthetic spectrum, taking column densities of 1.3×10^{15} and 4×10^{13} cm^{-2} toward the SW and NE images respectively, and a rotation temperature of 5.14 K.

B.2. HCN, HNC and HCO^+

Molecular absorption was first reported toward PKS 1830−211 by Wiklind & Combes (1996b) after the detection of the HCN, HNC, and HCO^+ 2-1 transitions, allowing the redshift of the intervening galaxy to be derived. Fig.B.2 shows the full spectra of the HCO^+, HCN, and HNC 1-0 transitions observed in our survey. The first two lines are likely saturated and their opacities could be underestimated. In particular two findings seem to indicate that the HCO^+ column density might be underestimated by a factor of 2-3. First, the $HCO^+/H^{13}CO^+$ ratio toward FG0.89SW is a factor of ∼2 lower than the corresponding $HCN/H^{13}CN$ and $HNC/HN^{13}C$ ratios. Second, the ratio of the column densities along the two lines of sight, SW/NE is also a factor 2-3 lower for HCO^+ than for other species (see Table 5). In any case, the uncertainty in the opacity introduced by the uncertainty in the continuum background illumination is nevertheless large for both HCO^+ and HCN (see §.3.3)

Time variations and the discovery of additional velocity components are discussed in §.3.2 and §.3.5, respectively.

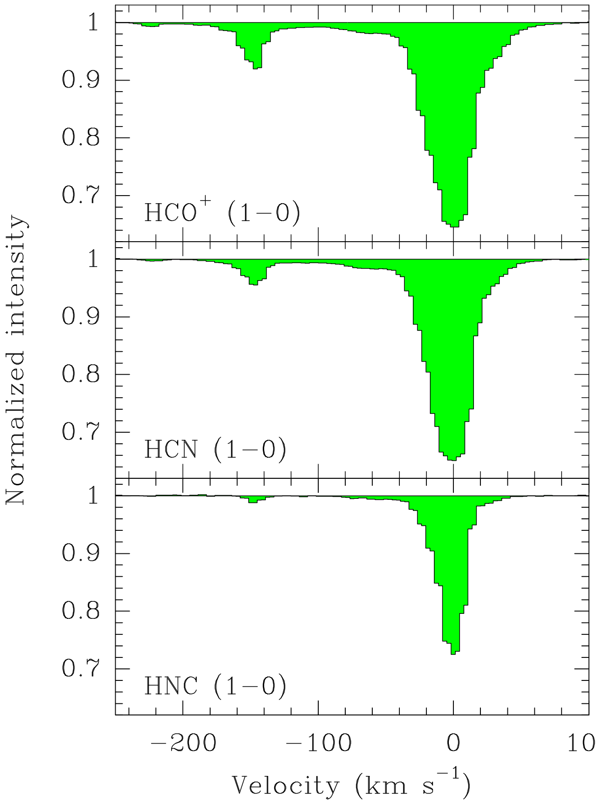

Fig. B.2. Full spectra of the HCO^+, HCN, and HNC 1-0 transitions, showing the absorption toward the SW (0 km s^{-1}) and NE (−147 km s^{-1}) images of the quasar. A zoom in with a narrower intensity scale, shown in Fig.6, reveals additional velocity components.

B.3. N_2H^+

N_2H^+ is thought to be one of the most abundant interstellar ions, and plays a key role in nitrogen chemistry. It is detected in a large number of Galactic clouds. However, it remains elusive in diffuse clouds (Liszt & Lucas 2001), with an abundance upper limit more than two orders of magnitude lower than its abundance in FG0.89SW. We note that N_2H^+ is also rare in translucent clouds, e.g., Turner (1995a) having detected it in only 2 out of 16 such clouds.

B.4. HOC^+

The hydroxymethylidynium ion, HOC^+, isomer of the formyl ion, was first tentatively identified in Sgr B2 by Woods et al. (1983). Its presence in several dense molecular clouds was then confirmed by Ziurys & Apponi (1995) and Apponi & Ziurys (1997), with a relative abundance $HCO^+/HOC^+ \sim 360$–6000. This abundance ratio is however about one order of magnitude lower ($\sim$70–120) in diffuse clouds (Liszt et al. 2004), and seemingly has an in-between value in PDR: Apponi et al. (1999) derived $HCO^+/HOC^+ \sim 270$ toward the Orion bar. Martín et al. (2009) find a ratio $\sim$70 toward NGC253, similar to that in diffuse clouds.

In FG0.89SW, we derive a ratio HCO^+/HOC^+ of $\sim$60, although this value might be slightly underestimated because of the large opacity of HCO^+. The $H^{13}CO^+/HOC^+$ ratio is indeed 2.6±0.1. Assuming a $^{12}C/^{13}C$ ratio of 35, the HCO^+/HOC^+ ratio in FG0.89SW is comparable to that in diffuse clouds.

B.5. HCO

The formyl radical, HCO, was discovered in the interstellar medium by Snyder et al. (1976) and has been identified as a tracer of the cloud-illuminated interface in PDRs (de Jong et al. 1980; Schilke et al. 2001). García-Burillo et al. (2002) revealed widespread HCO emission in the nuclear starburst of M82, with HCO, CO, and HII emission in nested rings, HCO extending farther out in the disk. Gérin et al. (2009) demonstrated that the HCO emission in the Horsehead nebula traces the PDR front, coincident with PAH and hydrocarbon emission. The abundance of HCO in the PDR is comparable to that of HCO^+, whereas it becomes about one order of magnitude less in the dense regions shielded from UV radiation. To the best of our knowledge, HCO has not been detected in diffuse or translucent clouds to date, although it is located close in frequency to the $H^{13}CO^+$ (1-0) and SiO (2-1) lines.

We clearly detect three (out of the four) hyperfine components of the ground state transition $1_{01} - 0_{00}$, the remaining low intensity component being buried in the noise level. The relative optical depths are consistent with LTE intensities, suggesting that the lines are optically thin. We derive an abundance ratio HCO^+/HCO of $\sim$13, similar to the values observed in dense shielded regions. This value is even larger if we consider that the HCO^+ opacity might be underestimated by a factor 2–3.

B.6. CH_2NH

We identify the absorption feature near 33.93 GHz with the $1_{01} - 0_{00}$ ground state transition of methanimine, as it is the simplest interstellar molecule with lowest energy transition close to that frequency. The hyperfine structure is not resolved. Only one line of methanimine is located within the limits of our frequency coverage. The strongest transitions, with predicted $\tau > 0.1$ based on the $1_{01} - 0_{00}$ absorption depth, have rest frequencies of 127.9, 166.9, 225.6 and 284.3 GHz. Of these, only the second and last fall in an ALMA band for a redshift of z=0.89.

Methanimine was first detected in Sgr B2 by Godfrey et al. (1973) and has been further observed in several star-forming regions and translucent clouds (Turner et al. 1999), but is not detected in cold dark clouds (Turner 1991; Dickens et al. 1997). It has been tentatively detected in NGC253 (Martín et al. 2006) and has been observed in Arp 220 (Salter et al. 2008). Methanimine is a prebiotic molecule, precursor to more complex molecules such as glycine.

B.7. CH_3NH_2

Methylamine is the saturated and terminal product of the hydrogenation series based on the cyanide radical: CN-HCN-CH_2NH-CH_3NH_2.

Methylamine has a very complex spectrum resulting from the combination of internal rotation of the CH_3 group, the asymmetry of the molecule and the inversion of the NH_2 group (Takagi & Kojima 1973; Ilyushin & Lovas 2007). It was first detected in Sgr B2 by Kaifu et al. (1974) (see also Turner 1991). No extragalactic detection has been reported to date.

B.8. CH_3OH

Interstellar methanol was first detected toward Sgr B2 and Sgr A by Ball et al. (1970) and is widely observed toward star forming regions, dark clouds, and also translucent clouds (Turner 1998). It has been detected in various extragalactic sources (e.g. Henkel et al. 1987). Methanol is about one order of magnitude less abundant in cold/translucent clouds than in star forming regions, where its abundance can reach a few 10^{-8} relative to H_2. It is not detected in diffuse clouds, down to upper limits of a few lower than its abundance in cold clouds (Liszt et al. 2008). Methanol is the terminal product of hydrogenation of CO.

The methanol spectrum has a multitude of transitions, of which only one is strong enough to be detected within our frequency coverage. Therefore, no excitation analysis can be deduced. Assuming LTE equilibrium with the CMB radiation field, we derive a relatively high methanol abundance of a few 10^{-8} relative to H_2 in FG0.89SW. Several strong lines (with predicted $\tau \sim 0.02$–0.4) near rest frequency of 300 GHz and redshifted in the 2 mm band are (simultaneously) observable (e.g. with ALMA or PdBI) and could provide a stringent measurement of the methanol rotation temperature.

The calculations of Jansen et al. (2011) have shown that methanol could be a sensitive probe of spatial and temporal variations in the proton-to-electron mass ratio.

B.9. l-C_3H

We identify the feature around 40.4 GHz with the J=7/2-5/2 transition of the $^2\Pi_{1/2}$ rotational ladder of the propynylidyne radical (ν_0=76.2 GHz). The transition is split into two Λ-doublets (see Fig.B.3), approximately equal in strength and spaced by about 5 MHz in the rest frame, which secures our identification. The hyperfine structure is unresolved. No other transitions of l-C_3H are detected in our frequency coverage.

Linear propynylidyne was first identified by Thaddeus et al. (1985a) toward IRC+10216 and TMC 1. It is observed in translucent clouds (Turner et al. 2000) but remains undetected in diffuse clouds (Lucas & Liszt 2000b, although this might just be a sensitivity issue, as their upper limits of l-C_3H/HCO^+ is still higher than the value we derive). No extragalactic detections have been reported to date that we are aware of.

The cyclic isomer form c-C_3H is detected in dense (Yamamoto et al. 1987; Fossé et al. 2001) and translucent (Turner et al. 2000) clouds, with c-C_3H/l-C_3H ratio ∼5. No transitions of c-C_3H are detected in our survey. In particular, the non-detection of the N_{KaKc}=2_{12}-1_{11} transition at a rest-frame frequency of 91.5 GHz, which is connected to the ground state, yields an upper limit of $\sim 3\times10^{12}$ cm^{-2}, and a c-C_3H/l-C_3H ratio <0.4. We note that a low ratio c-C_3H/l-C_3H< 1 was found by Turner et al. (2000) toward one translucent cloud (CB228).

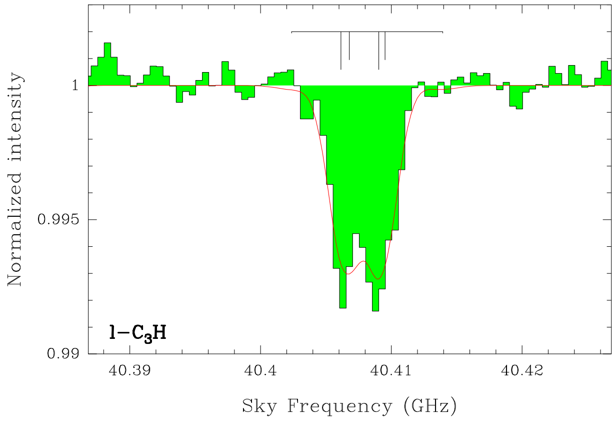

Fig. B.3. Spectrum of the l-C_3H J=7/2-5/2 transition. The locations of the two Λ-doublets with hyperfine structure are indicated.

B.10. c-C_3H_2

The ring molecule cyclo-propenylidene c-C_3H_2 is a fairly ubiquitous interstellar species (e.g., Thaddeus et al. 1985b; Matthews & Irvine 1985; Cox et al. 1988; Madden et al. 1989).

We detect 2 ortho and 2 para lines, yielding an ortho/para ratio of 2.8 ± 0.1, comparable to the statistical weight 3:1.

A tight correlation exists between the abundances of C_2H and c-C_3H_2 in diffuse clouds (Lucas & Liszt 2000b; Gérin et al. 2011), with $N(C_2H)=(28\pm1.4)N$(c-C_3H_2). We derive a comparable abundance ratio C_2H/c-C_3H_2=23.6 ± 0.2.

The excess absorption in the blue wing of the c-C_3H_2 2_{12}-1_{01} line (see Fig.B.4) could be due to the known velocity component at ∼−20 km s^{-1} toward FG0.89SW (see e.g. Fig.5 from Muller et al. 2006). Alternatively, we note that this feature could be due the HCS^+ 2-1 line, which would fall at ∼−32 km s^{-1} with respect to the center of the c-C_3H_2 2_{12}-1_{01} line. HCS^+ is indeed detected in diffuse clouds with an abundance of $\sim 3\times10^{-10}$ relative to H_2 (Lucas & Liszt 2002). If its abundance were similar in FG0.89SW, then the LTE predicted absorption depth would be of the order of τ=0.015, i.e. compatible with the observations. There are no other lines of HCS^+ within our frequency coverage. Observations of the J=1-0, 3-2, or 4-3 transitions (redshifted to 22.6, 67.9, and 90.5 GHz, and with predicted opacity of τ=0.007, 0.013, and 0.006, respectively) could confirm the presence of HCS^+.

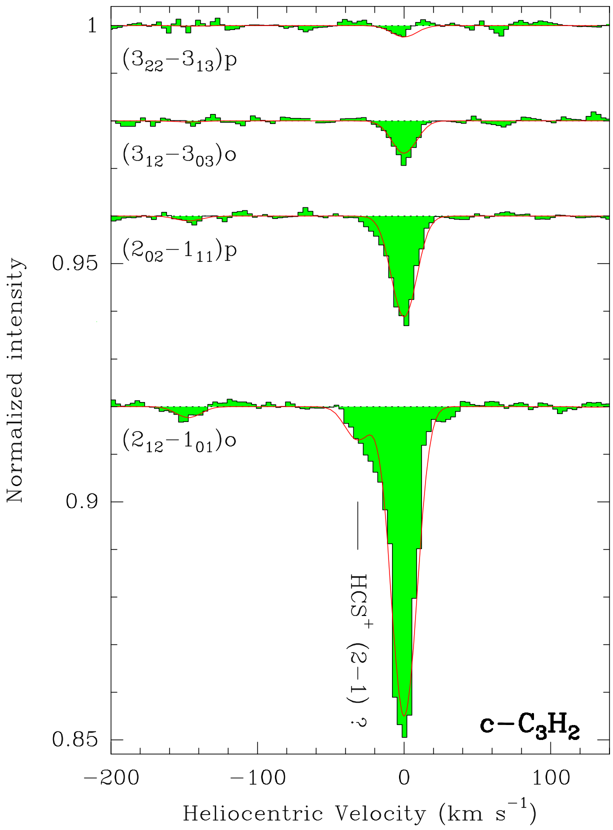

Fig. B.4. c-C_3H_2 transitions. The dashed curve on the wing of the $2_{12}-1_{01}$ line corresponds to the LTE prediction for the HCS^+ J=2-1 line with a HCS^+ column density of 5×10^{12} cm^{-2}.

B.11. l-C_3H_2

Propadienylidene, l-C_3H_2, is the linear isomer of c-C_3H_2 that was first discovered by Cernicharo et al. (1991) in the carbon-chain rich dark cloud TMC 1. Noticeably, Maier et al. (2011) identified l-C_3H_2 as the probable carrier of two conspicuous diffuse interstellar bands (at 4881 and 5450 Å).

The ortho/para ratio is $2.4^{+1.0}_{-0.5}$, in agreement with the statistical weight of 3:1.

The linear form is usually less abundant than the cyclic one, with a cyclic/linear ratio of 3–5 in diffuse clouds, 70 in TMC 1, and >150 in Sgr B2 (Cernicharo et al. 1991, 1999, see also Turner et al. 2000). We derive a cyclic/linear ratio of 25 ± 3, which is in-between the ratio observed toward diffuse clouds and TMC 1.

B.12. H_2CCN

The non-linear cyanomethyl radical has a very complicated spectrum owing to the unpaired electron and hyperfine splitting induced by the H and N atoms. We detect two absorption features, corresponding to N_{K_a,K_b}=3_{03}-2_{02} and

4_{04}-3_{03}. Both are from the ortho species (ortho states are characterized by K_a even and para states by K_a odd).

Irvine et al. (1988) first identified H_2CCN toward Sgr B2 and TMC 1. It was also detected in the circumstellar envelope of IRC+10216 (Agúndez et al. 2008), but, to the best of our knowledge, it has not been observed toward other sources. In particular, this is the first extragalactic detection of this molecule.

B.13. CH_3CCH

Methyl acetylene was first detected in Sgr B2 and Orion A by Snyder & Buhl (1973). It is observed in dark clouds (e.g., Irvine et al. 1981) and has been detected in the nearby starburst galaxies NGC253, NGC4945 and M82 (e.g. Mauersberger et al. 1991; Wang et al. 2004).

We detect the J_K=5_0-4_0 transition, but not the J_K=4_0-3_0, suggesting that the rotation temperature is higher than 5.14 K. The kinetic temperature was fixed to 50 K (see B.14).

We note that CH_3CCH is the molecule in our survey which shows the miminum scatter in relative abundances between the different sources.

B.14. CH_3CN

Methyl cyanide was first detected in space toward the Galactic center by Solomon et al. (1971). It is commonly detected in hot cores (e.g. Olmi et al. 1993), where the heating from massive stars is thought to evaporate the products of grain surface chemistry. The abundance of CH_3CN in these regions of active star formation exceeds 10^{-9} relative to H_2 (e.g. Kalenskii et al. 2000). We note that CH_3CN is also observed in dark clouds (Matthews & Sears 1983) and has been detected in NGC253 (Mauersberger et al. 1991). On the other hand, CH_3CN is detected in neither diffuse (Liszt & Lucas 2001) nor translucent clouds (Turner 2000), with upper limits clearly lower than abundances in dark clouds.

Symmetric-top molecule are excellent temperature probes, because radiative transitions between the different K-ladders are forbidden, so that only collisional excitation is effective. Consequently, the rotation temperature of the molecule can be derived within the same K-ladder on the one hand, and the kinetic temperature is reflected in the population of the K levels on the other hand (e.g. Churchwell & Hollis 1983).

In our LTE synthetic spectrum approach, the term $\exp\left(\frac{E_l}{k_B T_{rot}}\right)$ in Eq.2 was changed to $\exp\left[\frac{(E_l - E_{KK})}{k_B T_{rot}}\right] \exp\left[\frac{E_{KK}}{k_B T_{kin}}\right]$, where E_{KK} is the lowest energy level of each K-ladder, to evaluate the opacity of each transition (see e.g., Olmi et al. 1993). The partition function was calculated accordingly by taking into account both the rotation and kinetic temperatures

$$Q = \sum_{JK} g_I g_K g_J \exp\left(\frac{-(E_l - E_{KK})}{k_B T_{rot}}\right) \exp\left(\frac{-E_{KK}}{k_B T_{kin}}\right), \quad \text{(B.1)}$$

where g_J=(2J+1) and the product $g_I g_K$=2 for K=0 and $K \neq 3$n (n>0), and $g_I g_K$=4 for K=3n.

Two groups of transitions of methyl cyanide fall in the frequency coverage of our survey, the J_K=4_K-3_K redshifted near 39 GHz, and the J_K=5_K-4_K, redshifted to ∼48.8 GHz. Both are clearly detected. Remarkably, the K-ladder transitions are detected up to K=3 (see Fig.B.5), with lower energy state up to 70 K above the ground level. We note that CH_3CN is the only species in our survey showing absorption from such high energy levels. This suggests that the kinetic temperature is high, in agreement with the observations of inversion lines of ammonia up to (J,K)=10,10 (which lies at about 1000 K above the ground state) by Henkel et al. (2008). On the basis of their estimates, the kinetic temperature T_{kin} is about 80 K for 80-90% of the ammonia gas, while the remaining fraction could even reach T_{kin}>600 K.

A robust fitting of the CH_3CN spectra is difficult as the different K-ladder transitions are close in frequency relative to the width of the lines. Nevertheless, a good match of the observations could be found using our LTE model by assuming a CH_3CN column density of 1.3×10^{13} cm^{-2} and a kinetic temperature of 50 K (see Fig.B.5). This latter parameter value is comparable to, although slightly lower than that obtained by Henkel et al. (2008). We neglect the broadening of the line due to hyperfine splitting, as it is at most of 1.5 MHz for the principal hyperfine components of the J_K=5_4-4_4 transition.

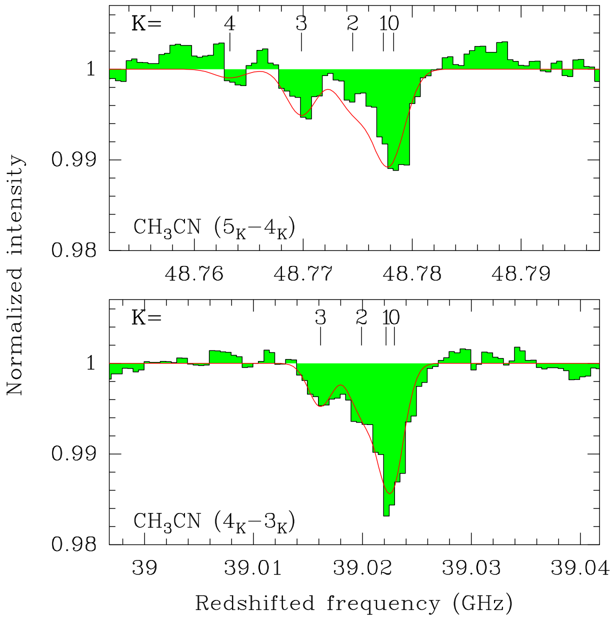

Fig. B.5. Spectra of the $4_K - 3_K$ and $5_K - 4_K$ transitions of CH_3CN. Our LTE prediction assuming a kinetic temperature of 50 K is overlaid.

B.15. H_2CCO

Ketene was first detected in Sgr B2 by Turner (1977). It was detected in line surveys of regions of low-mass and massive star formation (e.g. Turner 1991; van Dishoeck et al. 1995; Ruiterkamp et al. 2007), as well as in both translucent and dark clouds (Turner et al. 1999; Kaifu et al. 2004), suggesting that it is a common interstellar species. However, only few specific studies of the molecule have been conducted, and its formation mechanism(s) is subject to controversy: H_2CCO could be either produced by gas-phase reactions (Turner et al. 1999) or formed by means of surface chemistry, followed by grain desorption (Ruiterkamp et al. 2007). Its typical abundance is of the order of 10^{-10}–10^{-9} relative to H_2.

We detect four different (ortho) transitions of H_2CCO in our survey, yielding a rotation temperature of $2.6\,^{+1.1}_{-0.8}$ K, significantly lower than T_{CMB}=5.14 K at z=0.89.

B.16. HNCO

Isocyanic acid was first discovered toward Sgr B2 (Snyder & Buhl 1972). We detect two lines of HNCO, the 3_{03}-2_{02} and the 4_{04}-3_{03}, the latter in a low-noise region of the survey. They do not appear to be at LTE equilibrium, and we could not derive a positive rotation temperature. The centroid velocity of HNCO is also significantly offset with respect to the average velocity of all molecules. We could not identify lines from other molecules close in frequency, and therefore discard the possibility of a false identification.

B.17. SiO

Silicon monoxide is another commonly observed interstellar molecule, considered as a good shock tracer. Its abundance is low in cold dark clouds (of the order of or less than 10^{-12} relative to H_2), where it is presumably heavily depleted onto dust grains, but can reach values several orders of magnitude higher in outflows and shocked gas. It is found to have an intermediate abundance ($SiO/H_2{\sim}10^{-10}$) in diffuse and translucent clouds (Lucas & Liszt 2000a; Turner 2000). Toward FG0.89SW, we find a SiO abundance of nearly $4{\times}10^{-10}$ that is comparable to, though slightly higher than, that in diffuse/translucent clouds.

Interestingly, Ziurys et al. (1989) found a correlation between ln[SiO/HCN] and the inverse of the kinetic temperature in Galactic molecular clouds: were this correlation to hold for the gas in FG0.89SW, the SiO/HCN ratio would then point to a kinetic temperature of ∼30 K, a value not so far from the kinetic temperature estimated from CH_3CN.

The ^{29}SiO isotopologue is also detected and we derive a ^{28}Si/^{29}Si ratio of 11^{+4}_{-2}, which is roughly half the Solar System value.

B.18. CH_3CHO

Acetaldehyde is an asymmetric rotor, with two symmetry states (A and E) resulting from the rotation of the methyl group. Electric dipole transitions are not allowed between these states, which have the same weight statistic. Each transition is dedoubled by the symmetry, and the resulting spectrum consists of a series of closeby A/E doublets.

The detection of acetaldehyde was first reported toward Sgr B2 (Ball et al. 1971) and the molecule has been observed in cold dark clouds (Matthews et al. 1985) and translucent clouds (Turner et al. 1999). Interestingly, Chengalur & Kanekar (2003) observed that CH_3CHO is more widespread toward the Galactic center than most other complex organic molecules. They argue that the molecule could be produced by shock-induced disruption on dust mantles.

No extragalactic detection has yet been reported for this species.

B.19. NS

Nitrogen sulfide was first detected in Sgr B2 by Gottlieb et al. (1975). It is detected in quiescent clouds (McGonagle et al. 1994) and in massive-star forming regions (McGonagle & Irvine 1997). There are no reports of NS detection in diffuse or translucent clouds to date.

The rotational levels of the molecule are divided into two levels (e/f) with opposite parity by Λ-doubling, each of them subdivided into hyperfine structure corresponding to the nitrogen nucleus. We clearly detect the hyperfine components with highest relative intensities (see Fig.B.6). We note that the frequency interval between ∼36 and 40 GHz is the region observed with the lowest noise level in our survey, allowing these weak lines of NS, H_2CS, C_2S, and SO^+ to be detected.

Taking the CS column density estimated by Muller et al. (2006), we find a ratio NS/CS∼0.02, comparable to the values 0.02–0.05 measured by Hatchell, J. & Viti (2002) in a sample of hot cores. Martín et al. (2003) estimated a ratio NS/CS=0.4 in NGC253, which they interpreted as the signature of NS chemical enhancement by shocks (see also Viti et al. 2001).

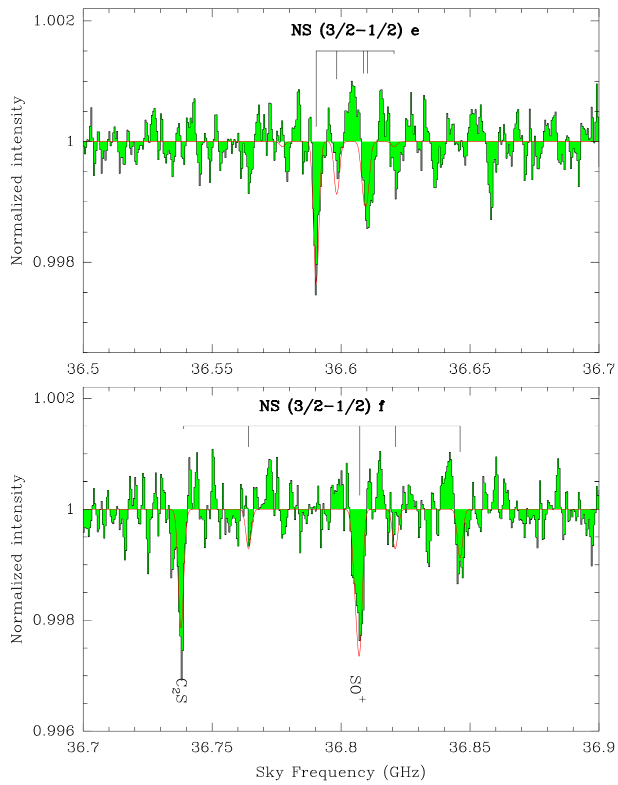

Fig. B.6. Spectrum of NS (2-1). The hyperfine structure with relative intensities is indicated.

B.20. H_2CS

Thioformaldehyde was first detected in absorption toward Sgr B2 by Sinclair et al. (1973). It is observed in star forming regions and cold dark clouds (e.g. Irvine et al. 1989; Minh et al. 1991) as well as in translucent clouds (Turner 1996). Tentative extragalactic detections are reported by

Heikkilä et al. (1999) in the LMC and Martín et al. (2006) in NGC253.

Two lines of H_2CS are detected, one of each ortho and para form, from which we derive an ortho/para ratio of $3.0^{+0.8}_{-0.5}$. However, we note that another ortho line, the 2_{12}-1_{11} at a rest frequency of 67.653820 GHz, should have been detected at the same intensity as the 2_{11}-1_{10} line, according to the LTE prediction. It is fitted with an opacity twice lower, although with a significance of just 3 σ on its integrated opacity, which is the reason we discarded it from our estimate of the ortho-H_2CS column density.

The H_2CO/H_2CS ratio, derived from their para forms, is 32±6, fully consistent with the present oxygen-to-sulphur cosmic abundance ratio (33:1, Lodders 2003).

B.21. SO

Sulfur monoxide was first detected by Gottlieb & Ball (1973) toward several star forming regions and later observed in dark clouds by Rydbeck et al. (1980).

From the J_K=2_1-1_0 line detected in our survey, we derive an abundance of $\sim10^{-9}$ relative to H_2, similar to that observed in Galactic diffuse clouds (Lucas & Liszt 2002), and ∼25 lower than that in translucent clouds (Turner 1995b).

The non-detection of the SO_2 1_{11}-0_{00} ground state transition yields a ratio $SO/SO_2>8$. Both species are observed in quiescent translucent clouds with an abundance ratio $SO/SO_2\sim1$–15 (Turner 1995b). It has been found that SO_2 is not detected in diffuse clouds, down to a fractional abundance $<10^{-9}$ (Lucas & Liszt 2002).

The non-detection of ^{34}SO points to an upper limit of $SO/^{34}SO>13.7$ (3σ). Muller et al. (2006) derived a ratio $^{32}S/^{34}S$ of 10.5 ± 0.6 from measurements of CS and H_2S, and their isotopologues.

B.22. SO$^+$

The reactive radical SO^+ is characterized by a $^2\Pi_{1/2}$ ground state. Its spin-doubled rotational transitions are split by Λ-type doubling.

The SO^+ J=3/2-1/2 e line is partly blended with the F=5/2-3/2 f hyperfine transition of NS. The width of the spectral feature at $\nu_{sky}\sim36.807$ GHz, as obtained by the fit of a single Gaussian component, is 37 ± 5 km s^{-1}, i.e. much larger than the width of other lines. Nevertheless, after taking into account the SO+ e/f doublet together with the NS line, the LTE synthetic spectrum reproduces fairly well the observations.

It has been found that SO^+ is a rather widespread and quite abundant interstellar species (Turner 1994), and is seen, although weakly, in translucent clouds (Turner 1996). There, the abundance ratio SO/SO^+ is of the order of 30. We estimate a ratio $SO/SO^+=15 \pm 3$ of comparable order of magnitude toward FG0.89SW.

B.23. C$_4$H

The butadiynyl radical was first reported by Guélin et al. (1978) toward IRC+10216 and has been observed toward dark clouds by Irvine et al. (1981). It is present in translucent clouds with a quite high abundance of a few 10^{-8} relative to H_2 (Turner 2000). No extragalactic detection has been reported so far.

The interaction of the unpaired electron with the molecular rotation produces fine structure, which is divided further into (here unresolved) hyperfine structure by the proton spin. The resulting spectrum of C_4H consists of a series of closeby doublets, of which we detect four (N=6-5 to N=9-8) within the limits of our frequency coverage.

B.24. HC$_3$N

The highly unsaturated cyanoacetylene molecule was first detected in Sgr B2 (Turner 1971) and is observed in various sources, such as translucent clouds, dense dark clouds, and star forming regions, with abundances of $\sim10^{-10}$–10^{-9} relative to H_2. HC_3N emission has also been detected in several extragalactic objects (see Lindberg et al. 2011 for a recent review).

We detect all four transitions of HC_3N within the frequency range of our survey, from J=7-6 to J=10-9. The J=3-2 and J=5-4 lines of HC_3N were previously detected with the VLA by Menten et al. (1999). More recently, Henkel et al. (2009) reported the detection of all transitions from J=3-2 to J=7-6 with the Effelsberg 100 m telescope. The J=10-9 line was not detected. The results of their observations are reported in the rotation diagram together with our data points (Fig.4). They appear to be inconsistent with one another. The integrated opacities of the J=7-6 line, observed in common with both works, differ by a factor of ∼2, as for their fitted linewidths. Time variablity and/or errors in the spectral baseline could explain the observed differences. We note that the higher S/N J=7-6 line appears slightly asymmetrical, with a shoulder on the blue-shifted side, reminescent of that of the HCO^+ 2-1 profile observed at higher spectral resolution (Muller et al. 2006; Muller & Guélin 2008). This transition was therefore not included in the Gaussian fit to derive the velocity and linewidth.

The points corresponding to the four lines observed by us appear remarkably well-aligned in the rotation diagram, suggesting that the lines are at LTE. They yield a rotation temperature of T_{rot}=6.3 ± 1.3 K, just slightly higher than the expected CMB temperature. On the other hand, the points corresponding to the lines observed by Henkel et al. (2009) at lower frequencies are not aligned in the rotation diagram. While we cannot discard possible time variations, another explanation could be a change in the source covering factor with frequency, as discussed by Henkel et al. (2009). Observations of all these transitions within a short period of time would help clarify the interpretation of these data.

B.25. C$_2$S

The thioxoethenylidene radical was first identified by Saito et al. (1987) in previous spectra of Sgr B2 and TMC 1, based on laboratory spectroscopy studies. It has been found that C_2S is present in translucent clouds (Turner et al. 1998) with a typical abundance of $\sim10^{-9}$ and is detected in the 2 mm survey of NGC253 by Martín et al. (2006). It is the heaviest species detected in our survey. We measure an abundance of $\sim2\times10^{-10}$ relative to H_2.

Few lines ($10 \geq J_u \geq 16$) of C_3S fall within the frequency coverage of our survey. Their non-detection gives a (not tightly constraining) ratio C_2S/C_3S>0.7. Search for lower J transitions of C_3S would be more sensitive. Fuente et al. (1990) measured a typical abundance ratio C_2S/C_3S=5 in dark clouds.